Qu Zhipeng (Orcid ID: 0000-0002-7895-6470)

Evaluation of a high-resolution NWP model's simulated clouds using observations from CloudSat, GOES-13, and *in situ* aircraft

ZHIPENG QU[1,8*], HOWARD W. BARKER[1,2], ALEXEI V. KOROLEV[1], JASON A. MILBRANDT[2], IVAN HECKMAN[1], STEPHANE BELAIR[2], SYLVIE LEROYER[2],PAUL A. VAILLANCOURT[2], MENGISTU WOLDE[3], ALFONS SCHWARZENBÖCK[4], DELPHINE LEROY[4], J. WALTER STRAPP[5], JASON N. S. COLE[1], LOUIS NGUYEN[6], AND ANDREW HEIDINGER[7]

[1] *Environment and Climate Change Canada, Toronto, ON, Canada*

[2] *Environment and Climate Change Canada, Dorval, QC, Canada*

[3] *National Research Council Canada, Ottawa, ON, Canada*

[4] *Laboratoire de Météorologie Physique, CNRS/Université Blaise Pascal, Clermont-Ferrand, France*

[5] *Met Analytics Inc., Aurora, ON, Canada*

[6] *NASA Langley Research Center, Norfolk, VA, USA*

[7] *NOAA/NESDIS/STAR, Madison, WI, USA*

[8] *McGill University, QC, Canada*

Submitted: 30 Nov. 2017

Revised: xx xxxx xxxx

For publication in: *Q. J. Royal Meteorol. Soc.*

* *Corresponding author address*: Zhipeng Qu, Rm 912 Burnside Hall, 805 Sherbrooke St. W., Montreal, Quebec H3A 0B9, Canada

E-mail: zhipeng.qu@mail.mcgill.ca

Abstract

This study aimed to assess tropical cloud properties predicted by Environment and Climate Change Canada's Global Environmental Multiscale (GEM) model when run with the Milbrandt-Yau double-moment cloud microphysical scheme and one-way nesting that culminated at a (~300 km)^2 inner-domain with 0.25 km horizontal grid-spacing. The assessment utilized satellite and *in situ* data collected during the High Ice Water Content (HIWC) and High Altitude Ice Crystal (HAIC) projects for a mesoscale convective system on 16 May 2017 over French Guiana. Data from CloudSat's cloud-profiling radar and GOES-13's imager were compared to data either simulated directly by GEM or produced by operating on GEM's cloud data with both the CFMIP (Cloud Feedback Model Intercomparison Project) Observation Simulator Package (COSP) instrument simulator and a 3D Monte Carlo solar radiative transfer model. *In situ* observations were made from research aircraft - Canada's National Research Council Convair-580 and the French SAFIRE Falcon-20 - whose flight paths were aligned with CloudSat's ground-track. Spatial and temporal shifts of clouds simulated by GEM compared well to GOES-13 imagery. There are, however, differences between simulated and observed amounts of high and low cloud. While GEM did well at predicting ranges of IWC near 11 km altitude (Falcon-20), it produces too much graupel and snow near 7 km (Convair-580). This produced large differences between CloudSat's and COSP-generated radar reflectivities and two-way attenuations. On the other hand, CloudSat's inferred values of IWC agree well with *in situ* samples at both altitudes. Generally, GEM's visible reflectances exceeded GOES-13's on

account of having produced too much low-level liquid clouds. It is expected that GEM's disproportioning of cloud hydrometeors will improve once it includes a better representation of secondary ice production.

Key words: Clouds, Microphysics, Mesoscale, Severe weather, Tropics, Numerical methods and NWP, Remote sensing, Field campaigns

1. Introduction

When jet-aircraft encounter large numbers of small ice crystals, notably at cruising altitudes in mesoscale convective systems (MCSs), engine effects such as surge, flame-out, vibration, damage, and uncontrolled power loss can ensue (Mason et al. 2006a). Regions with cloud ice water content (IWC) > 1 g m^{-3} have been identified as hazardous environments for commercial aircraft (Lawson et al. 1998; Mason et al. 2006b, Bravin et al., 2015). Statistical description of cloud microphysical properties and origins of regions with high IWC in MCSs were the foci of recent investigations by the joint-European High Altitude Ice Crystals (HAIC) (Dezitter et al. 2013) and North American High Ice Water Content (HIWC) projects (Strapp et al. 2016); both address concerns of the aviation industry and safety regulation. Their goals are, in part, to establish methods that provide early identification of cloud environments with high IWC thereby opening the possibility of procedures for commercial aircraft to avoid hazardous high IWC conditions.

While satellite-based diagnostic methods that aim to identify high IWC regions in MCSs are under development (e.g. Delanoë and Hogan, 2010; de Laat, 2017; Yost et al. 2018), an obvious alternate is advanced warning provided by numerical weather prediction (NWP) models. Although NWP model data has been used as input to one HIWC nowcasting scheme (Haggerty et al. 2012), the specific ability of NWP models to predict HIWC conditions has not been studied in detail. Of immediate and obvious concern is that less than adequate representations of cloud

processes in NWP models can be expected to have adverse impacts on the performance of potential warning tools that seek to identify regions of HIWC.

Despite recent advances, it is recognized widely that there is much room for improvement to both the representation and assessment of cloud, and associated processes, in NWP and global climate models (cf. Randall et al. 2003; IPCC 2013; Morrison and Milbrandt 2015). Hence, the main point of this study was to assess the ability of a high-resolution NWP model to predict HIWC conditions for tropical MCSs. The NWP model used here was Environment and Climate Change Canada's (ECCC) Global Environmental Multiscale (GEM) model (Côté et al. 1998; Girard et al. 2014), using one-way nesting that ended with $(300\ \text{km})^2$ domains whose horizontal grid-spacings were 0.25 km. Grid-scale clouds and precipitation processes were parametrized by Milbrandt and Yau's (2005) two-moment bulk microphysics scheme, and represented implicitly (subgrid-scale clouds) by parametrization schemes described in Bélair et al. (2005).

GEM's clouds were assessed using forward models that simulate satellite observations of GOES-13 geostationary visible reflectances and CloudSat cloud-profiling radar (CPR) reflectivities (Stephens et al. 2002) by operating directly on model-generated clouds (Bodas-Salcedo et al. 2011; Di Michele et al. 2012; Barker et al. 2017). This approach contrasts with methods that compare values of model-generated cloud variables to those inferred from satellite observations. GEM's simulated cloud variables were also compared to *in situ* measurements made by cloud sampling probes on two research aircraft - Canada's Convair-580 and France's Falcon-20 - that operated within the HAIC and HIWC projects in French Guiana

and whose paths were aligned with CloudSat's. Attention was paid to GEM's ability to simulate the existence, location, and magnitude of HIWC within an MCS that was sampled on 16 May 2015.

The next section provides a brief review of the high-resolution GEM NWP model and the simulation domain that straddled the coast of French Guiana. This is followed by a description of observed data from both satellite and aircraft. The fourth section discusses synthetic satellite data produced for GEM's clouds. These include CloudSat-like reflectivities produced by the CFMIP (**C**loud Feedback Model Intercomparison Project) Observation Simulator Package (Bodas-Salcedo et al. 2011; referred to hereinafter as the COSP simulator) and a 3D Monte Carlo solar radiative transfer (RT) model that simulated radiances commensurate with GOES-13 imagery. The Results section focuses on comparison of GEM data to observations of cloud IWC and ice particle number concentration. The final section offers a conclusion and summary of the study.

2. Global Environmental Multiscale (GEM) NWP model

The NWP model used in this study was Environment and Climate Change Canada's (ECCC) Global Environmental Multiscale (GEM) model (Côté et al. 1998; Girard et al. 2014). GEM's dynamics are formulated in terms of the non-hydrostatic primitive equations with a terrain-following hybrid vertical grid. It can be run as a global model (Barker et al. 2008) or a limited-area model and is capable of one-way self-nesting. Milbrandt et al. (2016) described the self-nesting configuration with horizontal grid-spacing $\Delta x \geq 2.5$ km; Leroyer et al. (2014) and

Bélair et al. (2017) did the same for $\Delta x \geq 0.25$ km. For the experiments reported here, four self-nested domains were used with areas of $(2{,}500 \text{ km})^2$, $(1{,}280 \text{ km})^2$, $(512 \text{ km})^2$, and $(300 \text{ km})^2$ with corresponding Δx of 10 km, 2.5 km, 1 km, and 0.25 km, respectively. The largest domain used 79 vertical layers while the others used 57, but with an increased number in the boundary-layer.

Milbrandt and Yau's (2005a,b) double-moment bulk cloud microphysics scheme (hereinafter referred to as MY2) was used. It predicts mass and number mixing ratio for each of six hydrometeors: non-precipitating liquid droplets; non-precipitating ice crystals; rain; snow; graupel; and hail. In this scheme, condensation (or ice nucleation) is formed only upon reaching grid-scale super-saturation with respect to liquid (ice) before microphysical adjustment. For liquid, saturation adjustment (removal of all supersaturation) is applied at each time-step, while for ice, explicit deposition/sublimation rates are computed. Each cloudy grid-cell is characterized by spatially uniform hydrometeor size distributions. Effective radii, defined as the ratio between the 3rd and 2nd moments of the hydrometeor size distribution, were derived from local mass and number, along with the assumption that size distributions follow complete gamma functions.

Apart from the MY2 scheme, the planetary boundary layer scheme can also produce cloud, namely cumulus and stratocumulus (Bélair et al. 2005). It predicts mean liquid and ice water contents as well as cloud fraction. The shallow convection scheme (Bélair et al. 2005) is the third means by which GEM can produce clouds. It predicts mean liquid and ice water contents and cloud fraction for cells that contain shallow cumulus clouds. Effective radii for liquid clouds

produced by the last two schemes are calculated assuming cloud droplet number concentrations of 500 cm^{-1} over land and 100 cm^{-1} over ocean. Ice crystal effective radii are set to 15 μm for radiative transfer calculations.

The simulation examined in this study was initialized with conditions from ECCC's global atmospheric analysis at 1200 UTC on 16 May 2015. The four one-way nested domains are centered at 4.68° N; 53.32° W as shown in Figure 1. Model fields were output and saved every 30 minutes between 1530 and 2100 UTC.

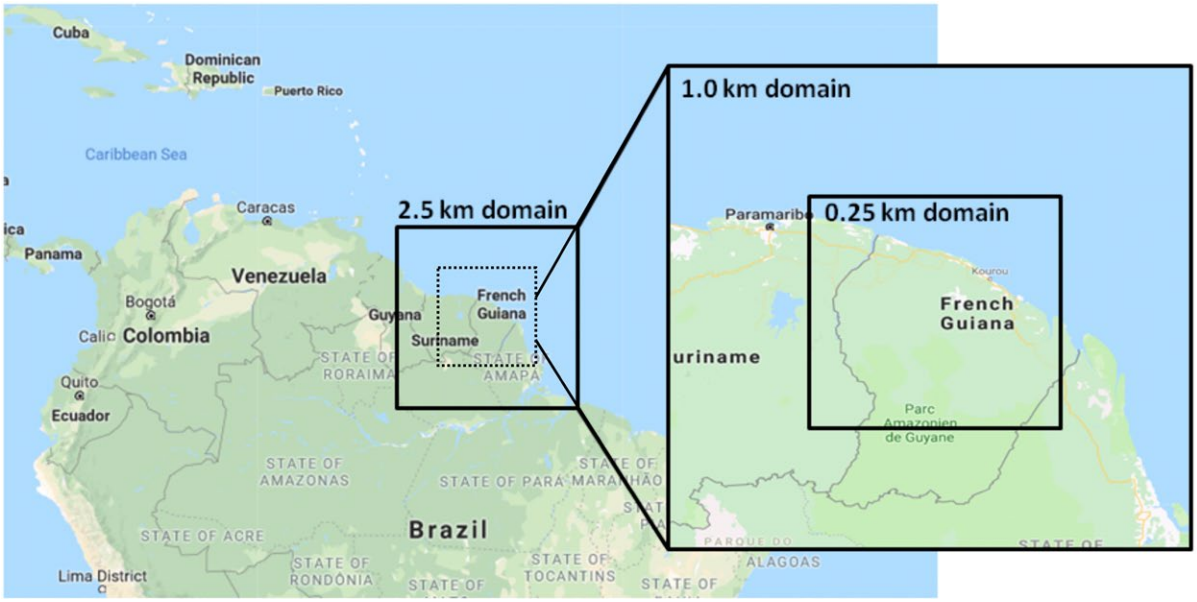

Figure 1. GEM's nested domains of areas $(1{,}280\ km)^2$, $(512\ km)^2$, and $(300\ km)^2$ which have Δx of 2.5 km, 1 km, and 0.25 km, respectively. Map source: Google Maps.

3. Observations

3.1. Aircraft data

In situ data employed in this study were collected from instruments on the NRC Convair-580 and SAFIRE Falcon-20 research aircraft. Both aircraft were stationed in Cayenne, French Guiana for the HAIC-HIWC campaigns (May 2015) and were equipped with state-of-art instrumentation for remote sensing and *in situ* characterization of cloud microphysical properties. Measured data for this study came from the Cloud Particle Probe (CDP) (Lance et al. 2010) and 2D imaging particle probes 2D-S (Lawson et al. 2006) and PIP (Baumgardner et al. 2001) which provided cloud particle size distributions (PSD) for particles between 2 □m and 6.4 enabled assessment of bulk microphysical characteristics of clouds, such as particle number concentration, extinction coefficient, and effective particle size. IWC was measured directly by the IsoKinetic Probe (Davison et al. 2008). All instruments were installed on both aircraft and their data were processed with equivalent methods and compared to ensure confidence. This approach minimized differences that could arise from data acquisition and post-processing by separate instruments and software, respectively.

On 16 May 2015 both aircraft were able to reach A-Train satellite ground-tracks. During CloudSat's overpass the Convair-580 flew at ~6.8 km in air temperatures T_a near -10°C. The Falcon-20 flew at ~10.5 km in T_a near -35°C. Figure 2 shows ground-tracks of CloudSat and the aircraft. CloudSat crossed the shown domain in ~24 s. At 17:18 UTC, the aircraft were flying

parallel to CloudSat's ground-track with westward offsets of 1.2 km for the Convair-580 and 1.6 km for the Falcon-20. The offsets were applied to avoid direct interference between the CloudSat and aircraft-mounted radars, although enhanced CPR reflection from the aircraft can be seen on CloudSat's Quicklook image for Granule 48139 (not shown here).

3.2. Satellite data

Visible and infrared imagery from GOES-13 geostationary satellite were used to assess the location and horizontal extent of the mesoscale convective system. Barker et al. (2017) analyzed the geometric properties of radiances associated with GOES-13 and GEM. CloudSat CPR reflectivities were used to assess vertical distributions of cloud. These data were compared directly to results from COSP operating on GEM data. IWC estimates from CloudSat's 2B-CWC-RO product (Austin et al. 2009) were compared to aircraft *in situ* measurements as well as values from GEM.

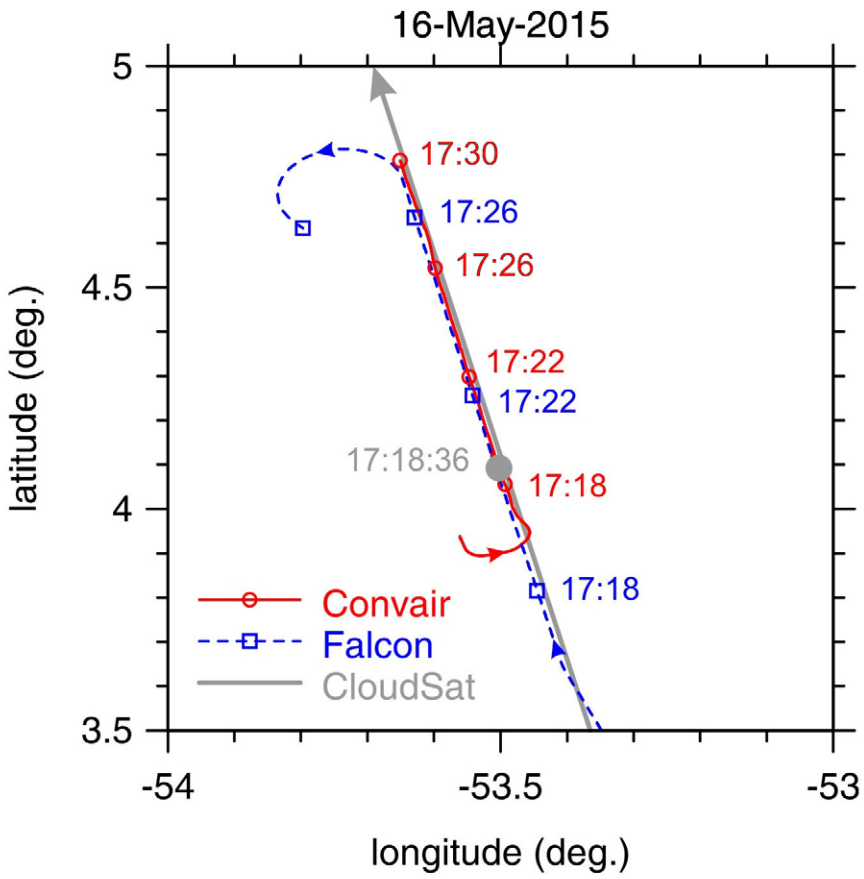

Figure 2. Ground-track for CloudSat as well as flight-paths for the Convair-580 and Falcon-20 across the central portion of GEM's inner-domain on 16 May 2015. Listed times are for the aircraft. CloudSat traversed this region in ~24 s and was over the Convair-580 at 17:18:36 UTC.

4. Simulated satellite observations for GEM

This section has two subsections, both of which discuss computation of approximate satellite observations corresponding to surface-atmosphere conditions produced by GEM. The first subsection pertains to CPR measurements while the second is for GOES-13 visible radiances.

4.1. CloudSat CPR

The CFMIP [(**C**loud Feedback Model Intercomparison Project) Observation Simulator Package] (Bodas-Salcedo et al. 2011), known as COSP, was applied to fields produced by GEM and yielded estimates of 94-GHz reflectivities commensurate with CloudSat's CPR (Stephens et al. 2002). COSP uses the QuickBeam algorithm (Haynes et al. 2007) to simulate CloudSat reflectivities. It assumes that: cloud mixing ratios in each model cell are uniform; size distributions, for spherical particles, follow gamma distributions; and columns are radiatively isolated regardless of Δx. Although radar returns can be impacted much by multiple scattering during heavy rain (> 3 to 5 mm h^{-1}), multiple scattering is neglected in this version of QuickBeam (Haynes et al. 2007). Hence, simulated radar reflectivities will be underestimates.

4.2. GOES-13 (visible radiances)

To estimate radiances consistent with GOES-13's channel 1 (0.55 - 0.65 □m), GEM's cloud fields were operated on by a 3D Monte Carlo (MC) solar RT model (Barker et al. 2003). This model employs the local estimation technique (Marchuk et al. 1980), assumes cyclic horizontal boundary conditions, and tracks photons through scattering events until they are either absorbed

by a particle, molecule, or the surface, or exit the domain's top. Underlying surfaces were Lambertian with albedos equal to GEM's 0.25 - 0.7 μm band. Extinction by air molecules was included, but aerosols were not. Liquid cloud optical properties were based on Lorenz-Mie theory using PSDs described by a gamma distribution with effective radius reported by GEM. Optical properties for ice clouds were derived from Yang et al.'s (2013) theoretical functions using effective radii reported by GEM. See Barker et al. (2015) for details.

The $(300\ \text{km})^2$ domains received 4×10^8 randomly positioned photons. Simulated radiances were averaged up to 1 km to match GOES-13, and so each 1 km area received ~4,450 photons which yielded MC uncertainties of ~3%. To avoid effects due to cyclic horizontal boundary conditions, only radiances for the central $(256\ \text{km})^2$ region were used (cf. Barker et al. 2017).

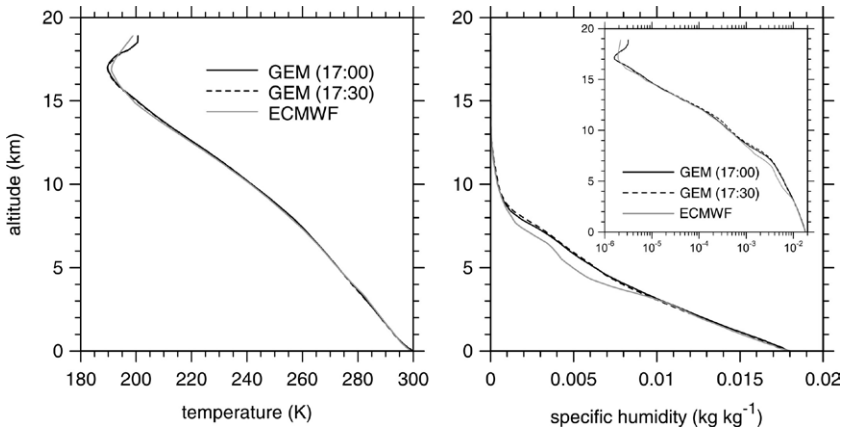

Figure 3**.** Profiles of air temperature and specific humidity from CloudSat's data files and GEM for 16 May 2015 (near 17:18 UTC). GEM's profiles are averages over cross-sections that

correspond to CloudSat's track shown in Figure 2. The inset plot's log-humidity scale accentuates small values above 12 km.

5. Results

Results are presented in two sub-sections. The first illustrates GEM's prediction of air temperature and humidity profiles. The second focuses on clouds and compares observations made by passive and active satellite sensors as well as aircraft *in situ* samples of cloud particles.

5.1. Meteorological conditions

At the most basic meteorological level, Figure 3 shows that, relative to ECMWF reanalysis (obtained from CloudSat's ECMWF_AUX files), GEM did well at simulating air temperature throughout the entire troposphere. This is not too surprising given the widespread and strong diurnal forcing of the tropical atmosphere. Likewise, it did equally well for humidity below and above ~3 km and ~9 km altitude, respectively, but it overestimated water vapour mixing ratio in the middle troposphere by often 30% - 40%. This sizable discrepancy can be expected to have ramifications on simulated clouds which, as shown later, were both overly abundant and dense at these altitudes.

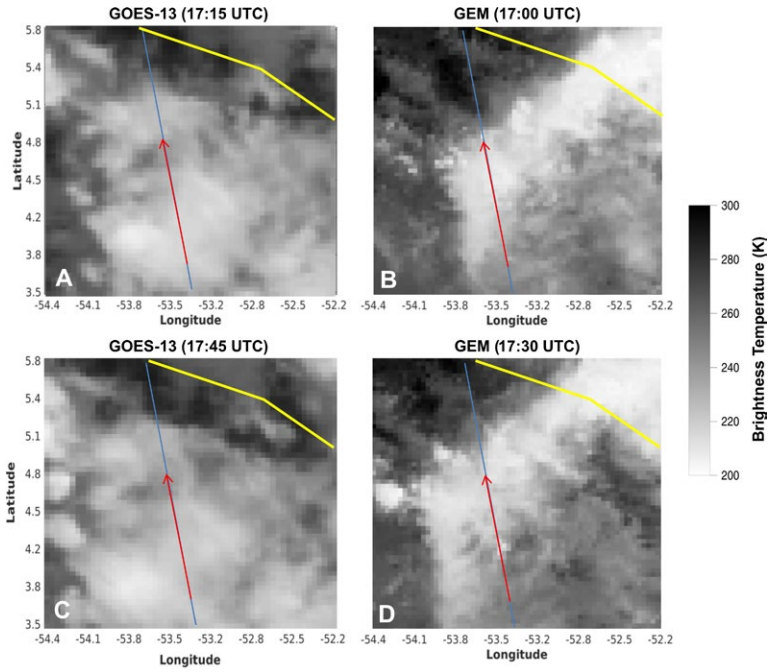

Figure 4: A: GOES-13 brightness temperatures, 4 km resolution for channel 4 (~11 □m), for 16 May 2015 at 17:15 UTC; B: corresponding GEM model field at 17:00 UTC; C: as in A except at 17:45 UTC; D: as in B except at 17:30 UTC. Blue and red lines represent the ground-tracks for CloudSat and the two aircraft. Yellow lines indicate South America's coastline.

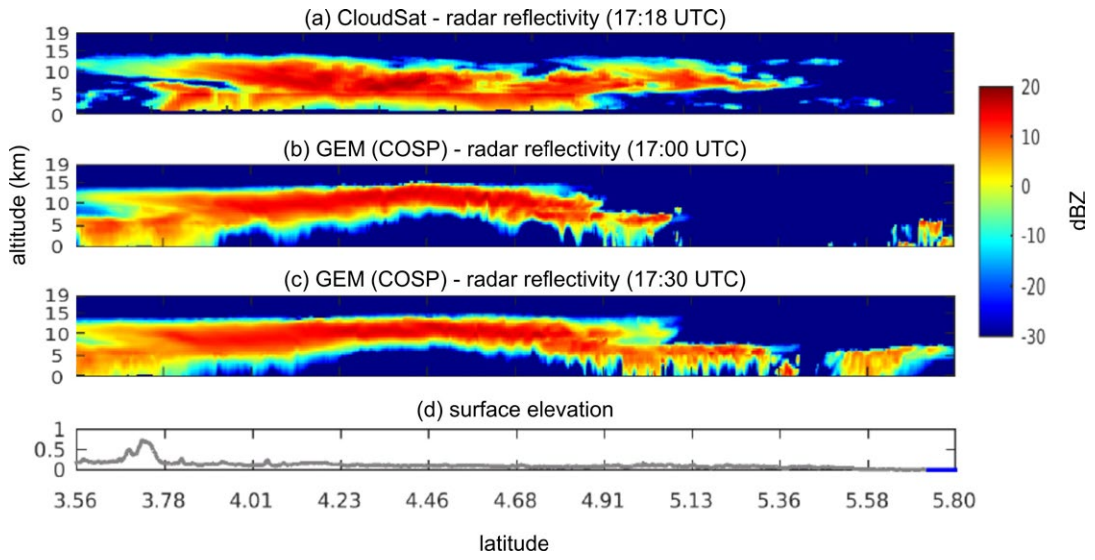

Figure 5: (a) CloudSat reflectivity profiles for 16 May 2015 at 17:18 UTC as a function of latitude. (b) and (c) COSP simulated CloudSat radar reflectivity for GEM's hydrometeors, along CloudSat's ground-track, for 16 May 2015 at 17:00 and 17:30 UTC. (d) Surface elevation and type (grey = land; blue = ocean).

5.2. Cloud conditions

Examination of 2D arrays of passive imagery reveals GEM's ability to capture large-scale aspects of cloud simulation such as position, advection rate, and vertically-integrated effective properties that influence radiances. Figure 4 shows effective radiating temperatures T_B for GOES-13 and GEM just before and after the A-Train's overpass. Considering the nonlinear nature of the atmosphere and uncertain model inputs, spatial and temporal displacements are expected for GEM's simulated variables. Visual comparison of GOES-13 images to GEM simulations revealed that GEM at 17:00 best resembles GOES-13 at 17:15 and the image of GEM at 17:30

resembles the best to the image of GOES-13 at 17:45. Therefore there is a 15 min gap between each comparison group. Along the A-Train ground-track, for both times shown, GOES-13 and GEM have minima T_B of 212 K and 207 K, respectively. Figure 5 shows that near 4° N GEM's cloud tops were at ~14 km, which corresponds well with CloudSat's. As such, GEM's T_B, of ~210 K, agrees nicely with GOES-13's, and because the upper-level clouds were quite dense, these T_B values almost match air temperatures at these altitudes (see Figure 3).

On the other hand, between approximately 4.4° N and 4.8° N GEM's cloud tops exceed CloudSat's by almost 2.5 km, and so its T_B values are often 15 - 20 K colder than CloudSat's. This is again consistent with air temperature profiles shown in Figure 3. Conversely, near 5.1° N GEM's clouds end abruptly and T_B values jumps to almost 300 K, while GOES-13's T_B values remain down near 230 K, corresponding to air temperatures near 11.5 km, just below CloudSat's cloud tops of ~12 km. These observations indicate that, at least along A-Train's ground-track there is consistency between general placement of cloud tops and temperature profiles.

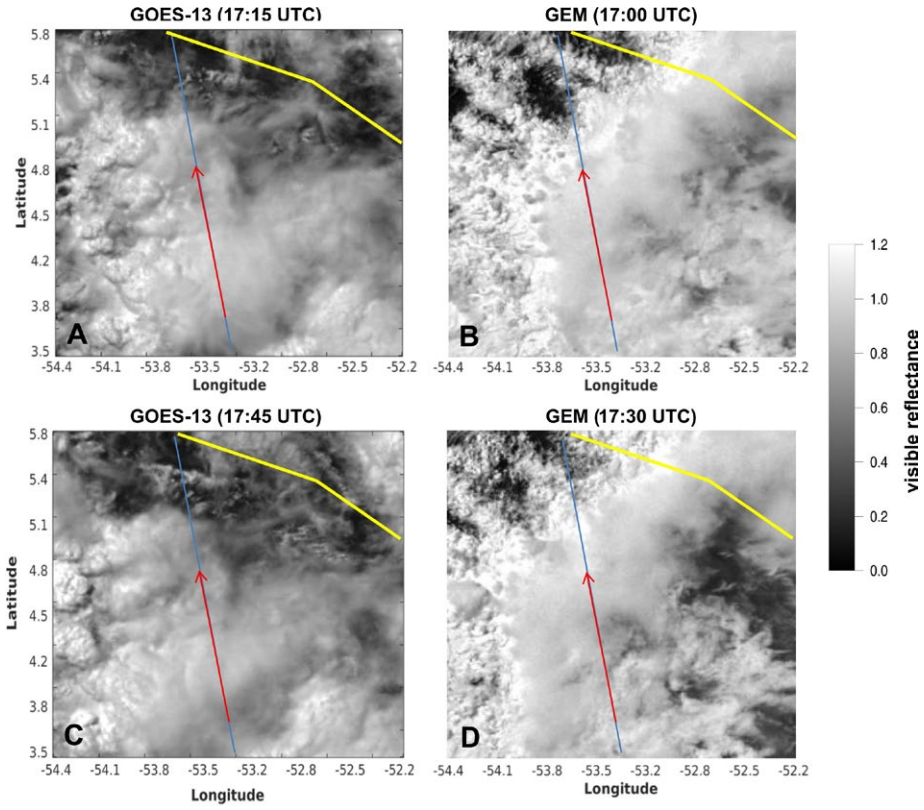

Figure 6: A: GOES-13 visible reflectances, 1 km resolution for channel 1, for 16 May 2015 at 17:15 UTC; B: corresponding TOA reflectances for GEM field at 17:00 UTC; C: as in A except at 17:45 UTC; D: as in B except at 17:30 UTC. Blue and red lines represent the ground-tracks for CloudSat-CALIPSO and the two aircraft. Yellow lines indicate South America's coastline.

What Figure 4 also indicates is that over the entire domain, GEM's upper-level clouds were too dense when they occurred, but their areal extent was too small. This is corroborated, somewhat, by Figure 6 which shows visible radiances for GOES-13 and GEM. It is clear by

simple visual inspection that the area of upper-level ice cloud is more extensive for GOES-13. What is more striking, however, and not apparent from Figure 3, is the expanse of dense, highly reflective, low-level clouds for GEM. With T_B values around 273 K, these are obviously liquid clouds which show-up nicely in Figure 5 between $5.1°$ N and $5.3°$ N. Note that the COSP simulator does not have the ability to affect a melting-layer bright-band, the sudden step-up in reflectivity due to droplets is apparent. Figure 7 shows the extent to which GEM's clouds out-reflected GOES-13's. At 1700 and 1730 UTC GEM had far too many very reflective clouds, while at 1730 UTC substantial areas of thin cloud appeared. By 1800 UTC, however, the thin areas persisted and the frequency of very bright clouds was diminishing. Throughout the hour, distributions of GOES-13 reflectances remained almost constant.

GEM's visible radiances were also computed assuming 1D RT. While the same model was used to compute 3D and 1D radiances, the latter used an arbitrarily large Δx which eliminated net horizontal transport of photons at all scales. As Figure 8 shows, visible radiances for 1D RT were "flat" compared to their 3D counterparts, and captured only a sense of a cloud-mask (cf. Barker et al. 2017). This is because 1D RT lacks shadowing and side illumination effects which are crucial to affect realistic imagery. This was not an issue for T_B values because: (i) they were measured and averaged up to 4 km resolution; and (ii) infrared radiances are much less sensitive than solar radiances to cloud structure.

A comparison of the positions of both deep convective and near-cloudless conditions at the two times shown in Figure 4 and Figure 6 indicates that both real clouds and GEM's clouds were

migrating westward at ~40 km h^{-1}. This shows, for this situation, GEM's clear ability to simulate accurately the lateral migration of clouds and active weather. The bigger issue, however, is getting the timing of occurrence in conjunction with both intensity and location. This is where it becomes difficult to compare directly to the single-pass of A-Train: the model might do fine in most respects, but if the timing of getting a certain set of conditions in the proper location fails, the assessment can be much compromised.

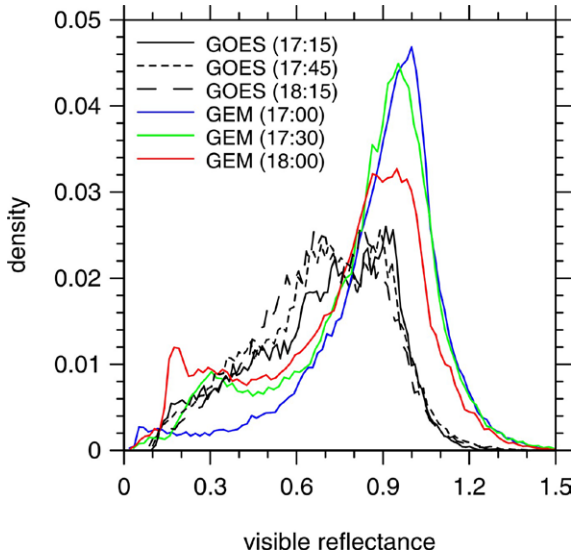

Figure 7: Probability densities of visible reflectance for GOES-13 and GEM images, as shown in Figure 6, at various times, near CloudSat's overpass as indicated in the legend.

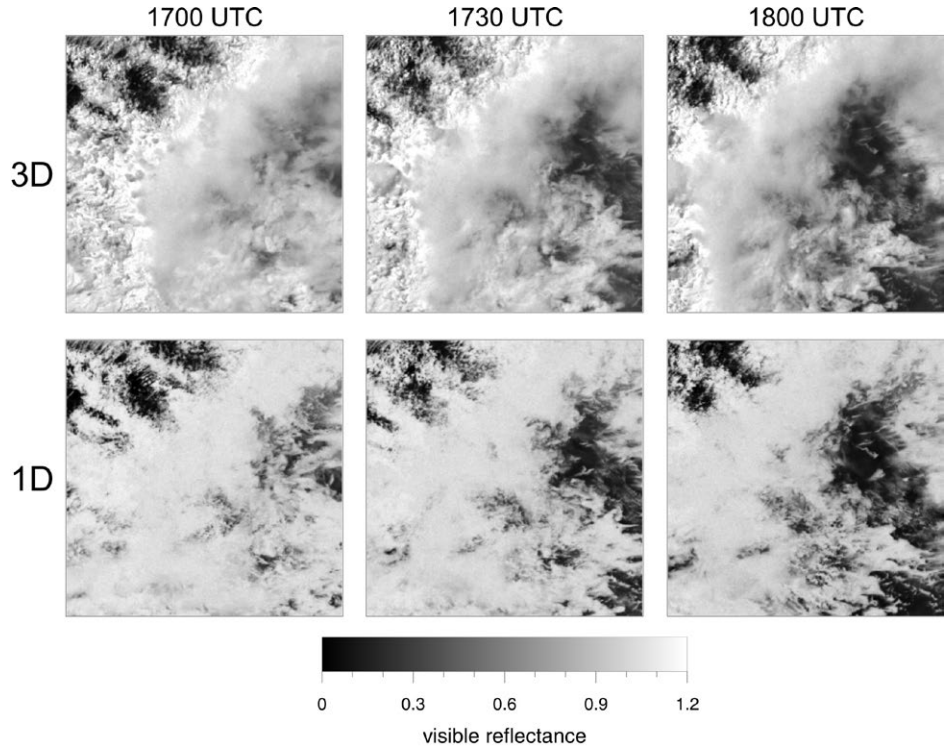

Figure 8: Upper and lower rows of images are visible radiances for GEM's clouds, at three times as listed, computed assuming 3D and 1D RT, respectively. While all images were computed using GEM's clouds resolved at 0.25 km horizontal grid-spacing Δx, and averaged up to 1 km resolution, the 3D and 1D RT simulations employed Δx = 0.25 km and 10^7 km, respectively.

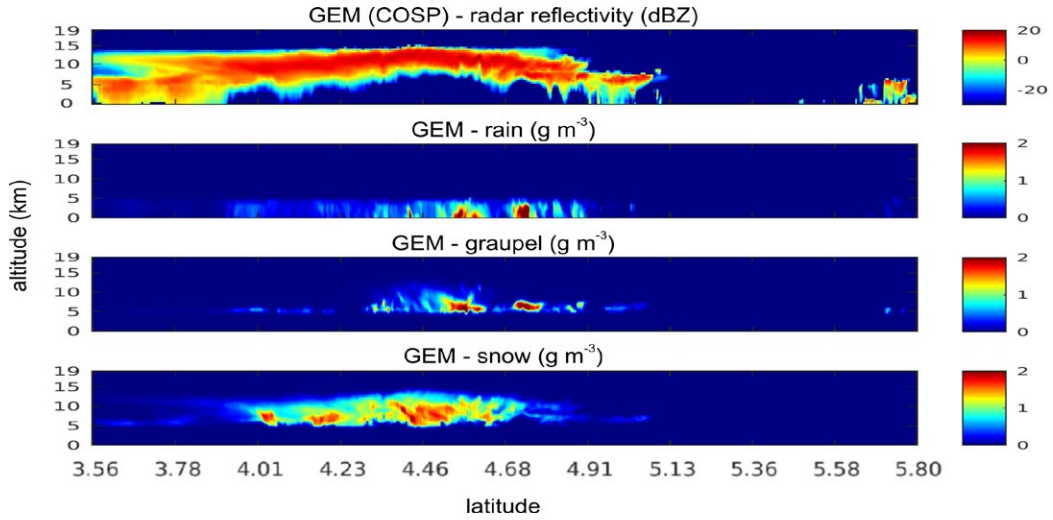

Figure 9: Upper panel shows COSP simulated CloudSat radar reflectivity for GEM's hydrometeors along CloudSat's ground-track for 16 May 2015 at 17:00 UTC. Lower panels show GEM's rain, graupel, and snow water contents.

Returning to Figure 5, perhaps the most striking feature is COSP's estimation of total attenuation of the CPR signal (i.e., returns smaller than -26 dBZ) between ~3.9° N and ~4.9° N. While there is what appears to have been substantial attenuation to CloudSat's signal in this location, it was nowhere near the total attenuation predicted by COSP. Moreover, where CloudSat seems to have experienced maximum attenuation is, as expected, directly beneath regions of relatively high reflectivities at altitudes between 5 km and 10 km. Although COSP indicates comparably high reflectivities up near 12 km, areas of total attenuation stemmed from horizontally widespread and vertically extensive integrated reflectivities. Figure 9 shows that heavy attenuation at 94 GHz was for regions with large amounts of graupel and snow which had

effective radii larger than 1.0 mm and 700 □m, respectively. Especially, the proposition of graupel among the solid categories is likely overestimated. Attenuation for COSP was, in fact, so severe that the curtains of maximum rain water content directly below areas of peak graupel and snow water contents went undetected. Equatorward of ~3.9° N the heavy attenuation aloft had lessened and so COSP produced some CPR returns down to the surface despite very light low-level rain.

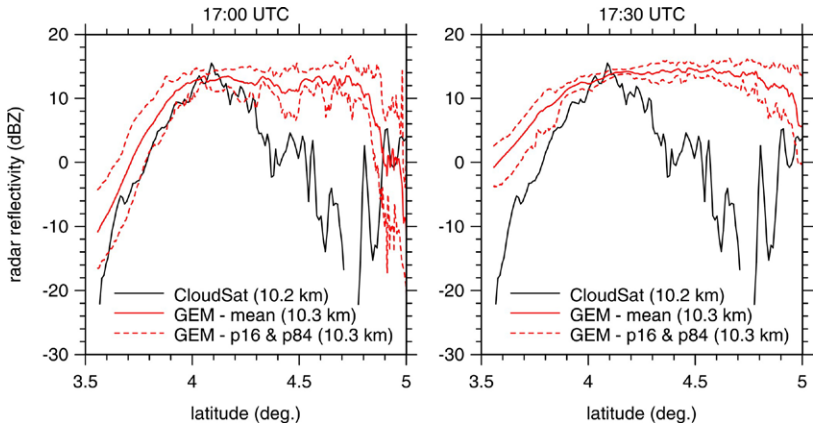

Figure 10. CloudSat radar reflectivity at altitude ~10.2 km as a function of latitude for 16 May 2015. Also shown is mean radar reflectivity simulated by COSP for a 40 km-wide swath of GEM data at altitude ~10.3 km, at 17:00 and 17:30 UTC, along CloudSat's track. Dashed lines, either side of the mean, are the 16th and 84th quantiles of COSP values for the 40 km-wide swath.

Regarding the likely scenario that sampling GEM fields along the A-Train track could lead to poor GEM comparisons because it misplaced hydrometeors exactly at overpass time, Figure 10

shows mean and standard deviation of COSP radar reflectivity at an altitude of ~10.3 km for a 40 km-wide swath about CloudSat's track for times that bracket the A-Train overpass. It also shows CloudSat's reflectivity at an altitude of ~10.2 km. This swath is meant to account for GEM's hydrometeors being misplaced by roughly ± 1/2 hour from CloudSat's overpass. South of ~ 4° N GEM-COSP values tracked CloudSat's fairly well in both magnitude and location. The same is true near 5° N. Between these locations, however, GEM-COSP values were consistently 10 – 20 dBZ too large; due, again, to GEM's overproduction of graupel and large snow particles.

In the South of ~4°N GEM-COSP radar reflectivity tracked CloudSat's fairly well though slightly overestimated. However, in this region the IWC values predicted by GEM are lower than those measured by the aircraft. One possible reason may be that GEM predicted larger ice particles comparing to what are observed at this level. Another reason might be due to the inherent assumption of ice particle size distribution. At this altitude, the ice particles are mostly very small. The assumed gamma distribution with its longer tail to the right side might slightly increase the number of lager ice particles.

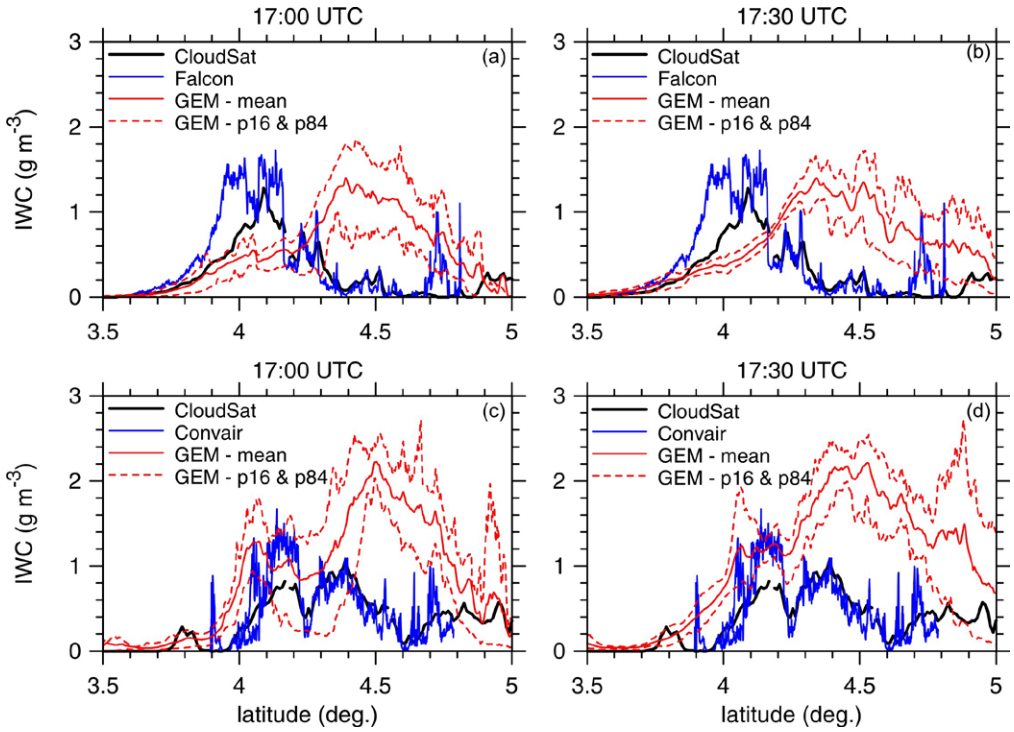

Figure 11. (a) and (b): IWC inferred from CloudSat reflectivities at altitude ~10.2 km as a function of latitude for 16 May 2015. Also shown is IWC measured on the Falcon-20 at ~10.5 km, as well as mean and the 16 and 84 percent quantiles of IWC as simulated by GEM at ~10.3 km for a 40 km swath about CloudSat's track. Values for both CloudSat and the Falcon-20 are the same at times 17:00 and 17:30 UTC; the times correspond to GEM. (c) and (d): The same as (a) and (b) except these correspond to altitudes near 6.8 km which was the Convair-580's altitude.

Another way to approach this is to look at inferred and measured values of IWC. Figure 11 compares IWC inferred from CloudSat's radar (Mace et al. 2006; Mace 2007) to *in situ* measurements made on two research aircraft that flew along the A-Train's track at, and around, overpass time. For the flight segment of concern, the aircraft were at altitudes of ~10.5 km (Falcon-20) and 6.8 km (Convair-580). CloudSat was over the aircraft at latitude ~4.1°N. Immediately to the south of that location both aircraft measured IWC values that were roughly 50 - 100% more than CloudSat's. They were, however, well away from CloudSat's track and only got onto it at ~4°N at approximately 5 minutes before overpass (see Figure 1). On the contrary, at overpass, and thereafter for ~70 km (~5 minutes beyond overpass), measurements made by both aircraft agree exceedingly well with CloudSat's and ranged from 0 to ~1 g m^{-3}.

Perhaps the most interesting aspect of the upper panel of Figure 11 is that GEM's maximum IWC values, at these altitudes along CloudSat's track, did not differ much from the maxima experienced by CloudSat and the aircraft; though the GEM maxima occurred ~50 km north of the CloudSat and aircraft maxima. A 40 km-wide averaging swath around the A-Train track was applied to account approximately for the stochastic nature of the problem, uncertain inputs, and approximations made within the GEM, all of which can be expected to yield temporal and spatial misplacements of simulated clouds. Additionally, the samplings were made around an A-Train track for 30 min before and after 17:00 UTC by shifting the track at 40 km h^{-1} in the dominant wind direction.

Figure 12 compares IWC values from CloudSat retrievals and aircraft *in situ* measurements to GEM's simulated mean values in the 40 km swath about the CloudSat track at 17:00 UTC and in the shifted domains 30 min before and after. Ranges and distributions of IWC are very similar for the three instances of simulated clouds. At the altitude of the Falcon (~10.3 km) there was a slight increase in IWC from 16:30 UTC to 17:00 UTC. This might be because of ongoing convections continually up-fluxing ice. From 17:00 UTC to 17:30 UTC IWC at ~10.3 km stayed relatively stable. At Convair altitudes (~6.8 km) peak IWC was stable for all three simulations. While these results provide a better illustration of errors in predicted clouds relative to more constrained averaging, results inferred from Figure 11 remain unchanged: GEM estimates the range of IWC at ~10.3 km quite well, but tends to overestimate IWC at ~6.8 km.

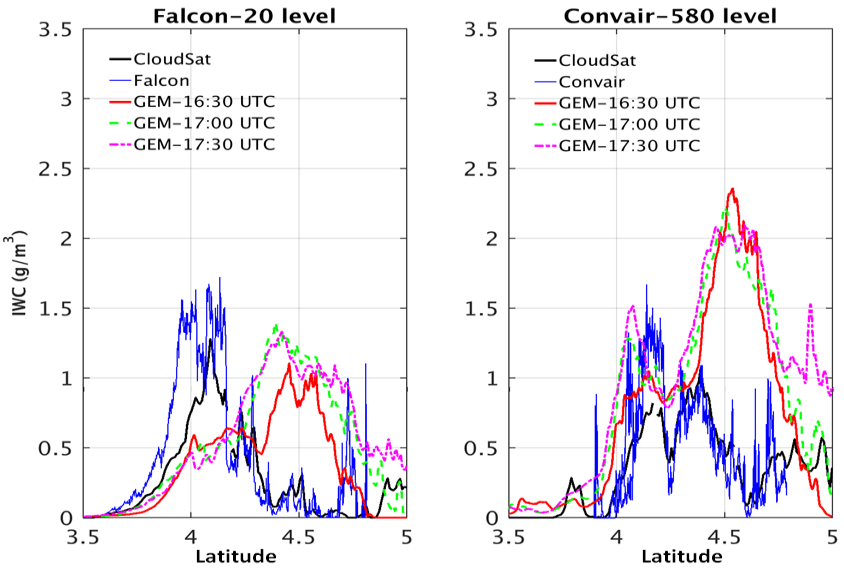

Figure 12. Left: IWC for CloudSat and Falcon along with GEM's mean IWC in the 40 km-wide swath at 17:00 UTC (CloudSat's passage) and for the shifted swaths at 16:30 UTC and17:30

UTC. Right: same as the left panel but showing CloudSat and Convair values and GEM's mean IWC at ~6.8 km.

Since a simulation's initial conditions and start time can be expected to impact predicted clouds, following additional simulations were conducted: one initiated at 12:00 UTC of the same day with analysis at a different cut-off time; and another initiated at 06:00 UTC. Figure 13 shows mean IWC in the 40 km swath about the CloudSat track for the original simulation (initiated at 12:00 UTC) and two additional simulations (initiated at 12:00 UTC and 06:00 UTC). The simulations initiated at 12:00 UTC give similar results at ~6.8 km; mean IWC values are overestimated by GEM regardless of differences in initial conditions. For mean IWC at ~11.3 km, the additional run yielded slightly smaller IWC with a similar spatial shift of the location of peak IWC; about 50 to 60 km to the north of the observed peak. The simulation initiated at 06:00 UTC produced a flat distribution of IWC throughout the domain. The range of IWC is similar to the observation at ~6.8 km though the simulated clouds are too extensive. Also, observed peak IWC near 4.2^{o}N is not captured by the model. At ~11.3 km the model largely underestimated IWC.

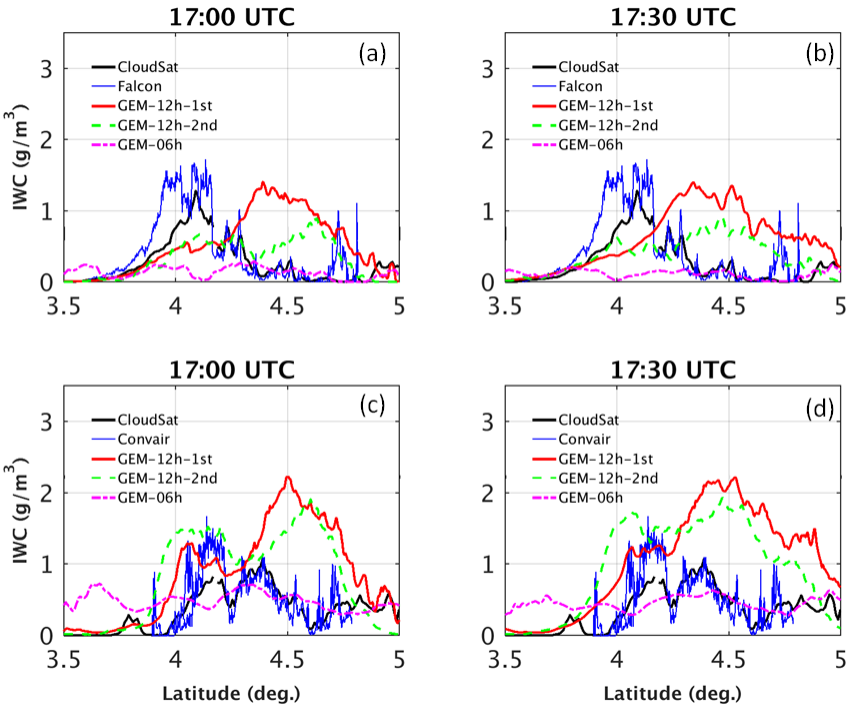

Figure 13. As Figure 11 except these show mean IWC for three GEM simulations: two runs starting at 12:00 UTC with slightly different initial conditions; and a simulation initialized at 06:00 UTC

Figure 13 also shows the impact of model lead time on the quality of predicted clouds. Both of the additional simulations produced clouds with similar characteristics: abundant, or at least sufficient, IWC at lower levels of the convective clouds, while at higher levels IWC is either slightly or strongly underestimated. This could be an indication that the vertical distribution of IWC tends to be more concentrated toward to the lower level at ~6.8 km.

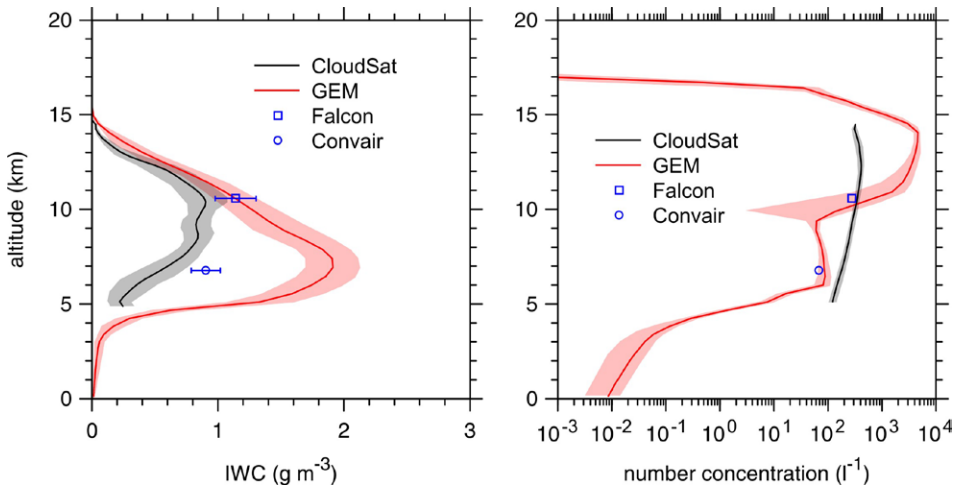

Figure 14. Lines and symbols represent mean IWC and ice particle number concentration profiles averaged over 4° N to 4.2° N for CloudSat and the aircraft, and 4.4° N to 4.6° N for GEM. GEM data are for 17:00 UTC. Shaded areas denote ranges between the 16th and 84th quantiles for CloudSat and GEM. Bars denote corresponding values for aircraft (for number concentrations, bars are approximately the width of the symbols). Quantiles for GEM and aircraft were computed for data degraded to CloudSat resolution (~1.2 km).

A similarity between the simulations initiated at 12:00 UTC is that locations of peak IWC are shifted northwards. So, perhaps GEM realized this system's most active region well except for its location? To look into this further, consider profiles of IWC for domains that approximately encompass the largest IWC values shown in Figure 11. Figure 14 shows IWC and ice particle

number concentrations averaged over 4°N to 4.2°N for CloudSat and the aircraft, and those values from the first run initiated at 12:00 UTC over 4.4°N to 4.6°N for GEM. Between 10 and 13 km, GEM's IWCs agree well with observations, in which the major fraction of GEM's IWC was snow. At the same altitudes GEM showed much higher number concentrations of particles; they were tiny ice crystals, with effective sizes near 20 – 30 □m, but with almost negligible contribution to IWC. Between altitudes of 5 - 10 km, however, CloudSat's IWC values were slightly less than those from aircraft, while GEM's were typically 2 - 3 times larger. Correspondingly, GEM's number concentrations agreed well with aircraft values, but CloudSat's values were 2 - 3 times larger. For most altitudes, values shown here are similar to those that have been reported elsewhere (e.g., Farrington et al. 2016). Those for GEM above ~12 km, however, were excessively large. Several reasons are possible for predicting these large values of number concentration such as the misrepresentation of ice initiation process, lack of dilution of the cloud environment by entrainment and mixing, difference between actual and modelled horizontal advection, spatial and temporal asynchronization of the modeled and actual processes.

The implication from Figure 14 is that GEM produces ice particles of much larger size than compared to those observed by aircraft and inferred from CloudSat at an altitude of ~7 km. There are several possible reasons for this and some, including excessive moisture between 4 and 9 km as shown in Figure 3, are under investigation. Of particular interest is the manner in which ice multiplication is treated in GEM. Currently, ice multiplication in MY2 is based on Hallett and Mossop's (1974) laboratory experiments. The number of ice particles produced by splintering is

supposed to be a function of ice rime mass and temperature. Recently, Lawson et al. (2015) explored a link between ice splintering and the size and number of freezing droplets in a given temperature range. Their approach is supported by evidence from aircraft *in situ* 2D imagery as well as laboratory high-speed photography (Wildeman et al. 2017).

In strong tropical convective updraughts there is a good chance of finding large numbers of large droplets at temperatures between -3°C and -15°C (or, following from Figure 3, at altitudes between ~7 km and ~9 km). According to Lawson et al. (2015), these droplets are likely to come into contact with ice nuclei and begin to freeze. During the freezing process some of the droplets will shatter into smaller fragments, while others can eject tiny ice particles (Wildeman et al. 2017). Since the number of new small ice particles is proportional to the fourth-power of droplet diameter (Lawson et al., 2015), ice number concentration increases dramatically. The current implementation of Hallett and Mossop (1974) is unable to quickly generate such high numbers of ice splinters. Thus, given the underestimated number concentrations near 7 km, GEM locally over-produced large ice particles which were, in turn, difficult to transport to higher altitudes by convective updraughts. This could explain why GEM's peak values of IWC occurred near 7 km, which is much lower than the 11 km observed and inferred by aircraft and CloudSat.

This study also points to some of problems that are inherent to cloud microphysics schemes (e.g., Milbrandt and Yau 2005a,b) that partition ice-phase hydrometeors into predefined categories such as "snow" and "graupel". Microphysics schemes being developed currently, however, are moving away from the fixed-category paradigm and focusing on prediction of bulk

ice properties. For example, Morrison and Milbrandt (2015) and Milbrandt and Morrison (2016) represent all ice-phase hydrometeors by one, or more, "free" categories, each of which can represent any type of frozen hydrometeor whose physical properties evolve smoothly via growth and decay processes. This eliminates the fictitious process of "conversion" between categories which is likely the source of problems in traditional schemes, as illustrated in this study where MY2 greatly over-predicted the mass of graupel. It is expected, therefore, that the next generation of microphysics schemes will yield better estimates of HIWC.

6. Conclusion

The underlying objective of this study was to begin testing the hypothesis that NWP model simulations can provide information used by commercial aircraft to avoid regions of high IWC that can compromise safe operation of jet engines. The first step toward this is to establish if NWP models are able to provide accurate estimates of high IWC with satisfactory spatial resolution and lead-time. This paper presented an evaluation of clouds simulated by ECCC's high-resolution GEM NWP model, in hind cast simulation mode, for a single case of tropical convection over French Guiana on 16 May 2015. GEM used an inner-domain D of $(300\ \text{km})^2$ at 0.25 km horizontal grid-spacing. On that day, D was positioned so as to include a cross-section of data collected by CloudSat's cloud-profiling radar. Moreover, two *in situ* sampling research aircraft, which were in the area for an international experiment related to aviation safety, under-flew CloudSat near the middle of D.

Results obtained here demonstrate GEM's capability at simulating tropical convective clouds. Spatial and temporal migrations of simulated clouds compared well to GOES-13 observations. There are differences between simulated and observed amounts of high and low clouds, though GEM did predict well the range of IWC near and above 11 km altitude. The model, however, tends to over-produce graupel and snow at intermediate altitudes near 7 km. One of the likely causes is GEM's overestimation of available moisture. Another possible cause for GEM's production of larger ice particles is poorly modelled secondary ice processes. It might be that the latter problem can be addressed by introducing new paramterizations of secondary ice production.

The COSP CloudSat simulator was applied to GEM's predicted cloud fields in order to generate 94 GHz radar reflectivities commensurate with CloudSat's. Also, to put GEM on a level field with GOES-13 imagery, which views D almost at nadir, a 3D Monte Carlo solar radiative transfer model operated on GEM's cloud fields and produced 1 km resolution visible radiances. When a 1D model was used to simulate visible radiances, GEM's fields lacked much texture and did not resemble GOES-13 imagery well. Infrared brightness temperatures for GEM fields were computed using a routine 1D radiative transfer model. This is because IR radiation is much less sensitive than visible radiation to fine details in cloud morphology, and also because GOES-13 IR radiances are resolved, and hence GEM averaged, to 4 km.

At the most basic level, GEM's simulated deep convection within D resembled closely what was seen by CloudSat and GOES-13; but the region of most active cloud development was

approximately 50 km too far north. A second simulation with the input analysis of different cut-off time showed a similar shift. This might be a systematic error of the model. However, GEM advected its clouds westward at rates close to what was observed by GOES-13.

Compared to GOES-13 visible radiances, those simulated for GEM were too reflective; largely on account of too much low-level liquid cloud. At the same time, however, because it predicted air temperature profiles well in conjunction with the densities of upper-levels clouds, its effective radiating temperatures were in much better agreement with GOES-13 values.

The most striking feature of GEM's COSP-simulated radar reflectivities was a heavy attenuation of the signal. While CloudSat's radar received return signals down to the surface across most of the 100 km-wide convective system, COSP experienced almost total attenuation below ~5 km. Such extreme attenuation stemmed from large amounts of simulated snow and graupel at altitudes between 5 and 10 km. These issues with GEM's simulation were confirmed by comparing its values of IWC and particle concentrations to those measured by aircraft at ~10 and ~7 km altitudes. It was hypothesized here that GEM's misaligned profiles of IWC and ice particle number concentration might be related to inadequate handling of secondary ice production processes which lead to predictions of too few, but too large, ice particles.

Taken together, GEM's misplacement of the region of most intense convection by ~50 km to the north, and its prediction of excessive IWC in the form of snow and graupel, near ~7 km suggests that, at the very least, more testing of GEM is needed before its estimates of IWC values can be considered to be reliable enough to be used in schemes to assist commercial

aircraft in avoiding hazardous HIWC conditions. A particularly promising avenue of work involves better treatment of secondary ice formation.

Acknowledgements

The authors thank Manon Faucher of Environment and Climate Change Canada (Dorval) for their help with running and analyzing the high-resolution GEM model. Major North American funding for HAIC-HIWC Cayenne-2015 flight campaign was provided by the FAA William Hughes Technical Center and Aviation Weather Research Program, the NASA Aeronautics Research Mission Directorate Aviation Safety Program, the Boeing Co., Environment Canada, the National Research Council of Canada, and Transport Canada. The HIWC/HAIC projects received funding from: (i) the European Union's Seventh Framework Program in research, technological development and demonstration under grant agreement n° ACP2-GA-2012-314314; (ii) the European Aviation Safety Agency (EASA) Research Program under service contract n° EASA.2013.FC27; and (iii) the Federal Aviation Administration (FAA), Aviation Research Division, and Aviation Weather Division, under agreement CON-I-1301 with the Centre National de la Recherche Scientifique. Additional support was provided by Airbus SAS Operations, Science Engineering Associates, the Australian Bureau of Meteorology, and Universities of Utah and Illinois.

References

Austin, R. T., A. J. Heymsfield, and G. L. Stephens, (2009) Retrieval of ice cloud microphysical parameters using the CloudSat millimeter-wave radar and temperature, *J. Geophys. Res*., **114**, D00A23, doi:10.1029/2008JD010049.

Barker, H. W., R. K. Goldstein, and D. E. Stevens, 2003: Monte Carlo simulation of solar reflectances for cloudy atmospheres. *J. Atmos. Sci*., **60**, 1881-1894.

Barker, H. W., J. N. S. Cole, J.-J. Morcrette, R. Pincus, P. Raisanen, K. von Salzen, and P. A. Vaillancourt, 2008: The Monte Carlo Independent Column Approximation: An Assessment using Several Global Atmospheric Models. *Q. J. R. Meteorol. Soc.* **134**: 1463–1478, doi:10.1002/qj.303

Barker, H. W., J. N. S. Cole, J. Li, B. Yi, and P. Yang, 2015: Estimation of Errors in Two-Stream Approximations of the Solar Radiative Transfer Equation for Cloudy-Sky Conditions. *J. Atmos. Sci*., **72**, 4053-4074, doi:10.1175/JAS-D-15-0033.1

Barker, H. W., Z. Qu, S. Belair, S. Leroyer, J. A. Milbrandt, P. A. Vaillancourt, 2017: Scaling Properties of Observed and Simulated Satellite Visible Radiances. *J. Geophys. Res.* **122**, 9413–9429, doi:10.1002/2017JD027146

Baumgardner, D., H. Jonsson, W. Dawson, D. O'Connor, R. Newton, 2001: The cloud, aerosol and precipitation spectrometer: a new instrument for cloud investigations. *Atmos. Res.*, **59–60**, 251–264, doi:10.1016/S0169-8095(01)00119-3

Bélair, S., J. Mailhot, C. Girard, and P. Vaillancourt, 2005: Boundary layer and shallow cumulus clouds in a mediumrange forecast of a large-scale weather system. Mon. Wea. Rev., **133**, 1938–1960, doi:10.1175/MWR2958.1.

Bélair, S., M. Roch, A. M. Leduc, P. A. Vaillancourt, S. Laroche, and J. Mailhot, 2009: Medium-range quantitative precipitation forecasts from Canada's new 33 km deterministic global operational system. *Weather and Forecasting,* **24**, 690–708. doi:10.1175/2008WAF2222175.1.

Bélair, S., S. Leroyer, N. Seino, L. Spacek, V. Souvanlasy, and D. Paquin-Ricard, 2017: Role and impact of the urban environment in the numerical forecast of an intense summertime precipitation event over Tokyo. In press: *J. Meteorol. Soc. Japan*.

Bodas-Salcedo, A., M. J. Webb, S. Bony, H. Chepfer, J. Dufresne, S. A. Klein, Y. Zhang, R. Marchand, J. M. Haynes, R. Pincus, and V. O. John, 2011: COSP: Satellite simulation software for model assessment. *Bull. Amer. Meteor. Soc*., **92**, 1023–1043, doi:10.1175/2011BAMS2856.1.

Bravin, M., J. W. Strapp, and J. Mason, 2015: An Investigation into Location and Convective Lifecycle Trends in an Ice Crystal Icing Engine Event Database. SAE Technical Paper 2015-01-2130, doi:10.4271/2015-01-2130.

Chepfer, H., S. Bony, D. Winker, M. Chiriaco, J.-L. Dufresne, and G. Sèze, 2008: Use of CALIPSO lidar observations to evaluate the cloudiness simulated by a climate model. *Geophys. Res. Lett.,* **35**, L15704, doi:10.1029/2008GL034207.

Côté, J., S. Gravel, A. Méthot, A. Patoine, M. Roch, and A. Staniforth, 1998: The operational CMC–MRD Global Environmental Multiscale (GEM) model. Part I: Design considerations and formulation. *Mon. Wea. Rev*., **126**, 1373–1395, doi:10.1175/ 1520-0493(1998)126,1373:TOCMGE.2.0.CO;2.

Davison, C., J. MacLeod, J. W. Strapp, and D. Buttsworth, 2008: Isokinetic total water content probe in a naturally aspirating configuration: Initial aerodynamic design and testing. Proc. 46th AIAA Aerospace Sciences Meeting and Exhibit, Reno, NV, American Institute of Aeronautics and Astronautics, AIAA 2008-435. [Available online at http://arc.aiaa.org/doi/abs/10.2514/6.2008-435.]

de Laat, A., E. Defer, J. Delanoë, F. Dezitter, A. Gounou, A. Grandin, A. Guignard, J. F. Meirink, J.-M. Moisselin, , and F Parol, 2017: Analysis of geostationary satellite-derived cloud parameters associated with environments with high ice water content. *Atmos. Meas. Tech*., **10**, 1359–1371, doi:10.5194/amt-10-1359-2017

Delanoë, J. and R. J. Hogan, 2010: Combined CloudSat-CALIPSOMODIS retrievals of the properties of ice clouds, *J. Geophys. Res*., **115**, D00H29, doi:10.1029/2009JD012346.

Dezitter, F., A. Grandin, J.-L. Brenguier, F. Hervy, H. Schlager, P. Villedieu, and G. Zalamansky, 2013: HAIC (high altitude ice crystals). Proc. *Fifth AIAA Atmospheric and Space Environments Conf*., San Diego, CA, American Institute of Aeronautics and Astronautics, AIAA 2013-2674. [Available online at http://arc.aiaa.org/doi/abs/10.2514/6.2013-2674.]

Di Michele, S., M. Ahlgrimm, R. Forbes, M. Kulie, R. Bennartz, M. Janisková, and P. Bauer, 2012: Interpreting an evaluation of the ECMWF global model with CloudSat observations: ambiguities due to radar reflectivity forward operator uncertainties. *Q. J. R. Meteorol. Soc.*, **138**: 2047–2065, doi:10.1002/qj.1936

Frey, W., S. Borrmann,D. Kunkel, R. Weigel, M. de Reus, H. Schlager, A. Roiger, C. Voigt, P. Hoor, J. Curtius, M. Krämer, C. Schiller, C. M. Volk, C. D. Homan, F. Fierli, G. Di Donfrancesco, A. Ulanovsky, F. Ravegnani, N. M. Sitnikov, S. Viciani, F. D'Amato, G. N. Shur, G. V. Belyaev, K. S. Law, and F. Cairo, 2011: *In situ* measurements of tropical cloud properties in the West African Monsoon: Upper tropospheric ice clouds, Mesoscale Convective System outflow, and subvisual cirrus, *Atmos. Chem. Phys*., **11**, 5569-5590, doi:10.5194/acp-11-5569-2011.

Farrington, R. J., P. J. Connolly, G. Lloyd, K. N. Bower, M. J. Flynn, M. W. Gallagher, P. R. Field, C. Dearden, and T. W. Choularton, 2016: Comparing model and measured ice crystal concentrations in orographic clouds during the INUPIAQ campaign. *Atmos. Chem. Phys.*, **16**, 4945–4966, doi:10.5194/acpd-15-25647-2015

Girard, C., M. Desgagné, R. McTaggart-Cowan, J. Côté, M. Charron, S. Gravel, V. Lee, A. Patoine, A. Qaddouri, M. Roch, L. Spacek, M. Tanguay, P. A. Vaillancourt, and A. Zadra, 2014: Staggered Vertical Discretization of the Canadian Environmental Multiscale (GEM) model using a coordinate of the log-hydrostatic-pressure type. *Mon. Weather Rev.*, **142**, 1183-1196, doi.org/10.1175/MWR-D-13-00255.1

Haggerty, J., F. McDonough, J. Black, G. Cunning, G. McCabe, M. Politovich, and C. Wolff, "A system for nowcasting atmospheric conditions associated with jet engine power loss and damage due to ingestion of ice particles," *4th AIAA Atmospheric and Space Environment Conf.*, New Orleans, LA, 25 – 28 June 2012, AIAA-2012-3234.

Hallett, J., and S. C. Mossop, 1974: Production of secondary ice particles during the riming process. *Nature*, **249**, 26–28, doi:10.1038/249026a0.

Haynes, J. M., R. T. Marchand, Z. Luo, A. Bodas-Salcedo, and G. L. Stephens, 2007: A multi-purpose radar simulation package: Quick-Beam. *Bull. Amer. Meteor. Soc.*, **88**, 1723-1727, doi:10.1175/BAMS-88-11-1723.

Intergovernmental Panel on Climate Change, 2013: Summary for policymakers. *Climate Change 2013: The Physical Science Basis*, T. F. Stocker et al., Eds., Cambridge University Press, 1–29.

Ladino, L. A., A. V. Korolev, I. Heckman, M. Wolde, A. M. Fridlind, and A. S. Ackerman, 2017: On the role of ice-nucleating aerosol in the formation of ice particles in tropical mesoscale convective systems, *Geophys. Res. Lett.*, **44**, 1574–1582, doi:10.1002/ 2016GL072455

Lance, S., C. A. Brock, D. Rogers, and J. A. Gordon, 2010: Water droplet calibration of the Cloud Droplet Probe (CDP) and in-flight performance in liquid, ice and mixed-phase clouds during ARCPAC, *Atmos. Meas. Tech.*, **3**, 1683–1706, doi:10.5194/amt-3-1683-2010.

Lawson, R. P., L. J. Angus, and A. J. Heymsfield, 1998: Cloud Particle Measurements in Thunderstorm Anvils and Possible Threat to Aviation. *J. Aircraft*, **35**, 113-121.

Lawson, P. R., D. O'Connor, P. Zmarzly, K. Weaver, B. Baker, Q. Mo, and H. Jonsson, 2006: The 2D-S (stereo) probe: Design and preliminary tests of a new airborne, high-speed, high resolution, particle imaging probe. *J. Atmos. Oceanic Tech.*, **23**, 1462–1477, doi:10.1175/JTECH1927.1.

Lawson, R. P., S. Woods, H. Morrison, 2015: The Microphysics of Ice and Precipitation Development in Tropical Cumulus Clouds. *J. Atmos. Sci.*, **72**, 2429–2445, doi:10.1175/JAS-D-14-0274.1.

Leroy, D., E. Fontaine, A. Schwarzenböck, J. W. Strapp, et al., 2015: HAIC/HIWC Field Campaign - Specific Findings on PSD Microphysics in High IWC Regions from *In Situ* Measurements: Median Mass Diameters, Particle Size Distribution Characteristics and Ice Crystal Shapes. SAE Technical Paper 2015-01-2087, doi:10.4271/2015-01-2087.

Leroyer, S., S. Bélair, S. Husain, and J. Mailhot, 2014: Subkilometer numerical weather prediction in an urban coastal area: A case study over the vancouver metropolitan area. *J. Appl. Meteor. Climatol.*, **53**, 1433?1453, doi:10.1175/JAMC-D-13-0202.1.

Mace, G. G., 2006: CloudSat project: Level 2 GEOPROF Product Process Description and Interface Control Document Algorithm version 5.3. Available at: http://cloudsat.cira.colostate.edu/dataICDlist.php?go=list&path=/2B-GEOPROF.

Mace, G. G. et al., 2007: CloudSat project: Level 2 Radar-Lidar GEOPROF Product VERSION 1.0 Process Description and Interface Control Document. Available at: http://cloudsat.cira.colostate.edu/dataICDlist.php?go=list&path=/2B-GEOPROF-LIDAR.

Marchuk, G. I., G. A. Mikhailov, M. A. Nazaraliev, R. A. Darbinjan, B. A. Kargin, and B. S. Elepov, 1980: *Monte Carlo Methods in Atmospheric Optics*. Optical Science Series 12, Springer-Verlag: Berlin and Heidelberg, Germany and New York, NY, 208 pp.

Mason, J. G., J. W. Strapp, P. Chow, 2006a: The Ice Particle Threat to Engines in Flight. *44th AIAA Aerospace Sciences Meeting and Exhibit*, 9 - 12 January 2006, Reno, Nevada, AIAA 2006-206, 21p.

Mason, J., J. W. Strapp, and P. Chow, 2006b: The Ice Particle Threat to Engines in Flight. *44th AIAA Aerospace Sciences meeting and Exhibit*, Reno, Nevada AIAA 2006-206.

Milbrandt, J. A., and M. K. Yau, 2005a: A multi-moment bulk microphysics parameterization. Part I: Analysis of the role of the spectral shape parameter. *J. Atmos. Sci.*, **62**, 3051–3064, doi:10.1175/JAS3534.1

Milbrandt, J. A., and M. K. Yau, 2005b: A multi-moment bulk microphysics parameterization. Part II: A proposed three-moment closure and scheme description. *J. Atmos. Sci.,* **62**, 3065–3081, doi:10.1175/JAS3535.1.

Milbrandt, J. A., S. Bélair, M. Faucher, M. Vallée, M. L. Carrera, and A. Glazer, 2016: The Pan-Canadian high resolution (2.5km) deterministic prediction system. *Weather and Forecasting*, **31**, 1791-1816, doi: 10.1175/WAF-D-16-0035.1.

Morrison, H. and J. A. Milbrandt, 2015: Parameterization of cloud microphysics based on the prediction of bulk ice particle properties. Part I: Scheme description and idealized tests. *J. Atmos. Sci*., **72**, 287-311, doi:10.1175/JAS-D-14-0065.1.

Randall, D. A., M. F. Khairoutdinov, A. Arakawa, and W. W. Grabowski, 2003: Breaking the cloud parameterization deadlock. *Bull. Am. Meteorol. Soc.*, **84**, 1547–1564 , doi:10.1175/BAMS-84-11-1547.

Strapp, J. W., A. V. Korolev, T. Ratvasky, R. Potts, A. Protat, P. May, A. Ackerman, A. Fridlind, P. Minnis, J. Haggerty, J. T. Riley, Lyle E. Lilie, and G. A. Isaac, 2016: The high ice water content study of deep convective clouds: Report on science and technical plan. DOT/FAA/TC-14/ 31. [Available at http://www.tc.faa.gov/its/worldpac/techrpt/tc14-31.pdf.]

Wildeman, S., S. Sebastian Sterl, C. Sun, and D. Lohse, 2017: Fast dynamics of water droplets933 freezing from the outside in. *Phys. Rev. Lett.*, **118**, 08410, doi:10.1103/PhysRevLett.118.084101

Yang, P., L. Bi, B. A. Baum, K.-N. Liou, G. Kattawar, M. Mishchenko, and B. Cole, 2013: Spectrally consistent scattering, absorption, and polarization properties of atmospheric ice crystals at wavelengths from 0.2 µm to 100 µm. *J. Atmos. Sci.*, **70**, 330-347, doi:10.1175/JAS-D-12-039.1

Yost, C. R., K. M. Bedka, P. Minnis, L. Nguyen, J. W. Strapp, R. Palikonda, K. Khlopenkov, D. Spangenberg, W. L. Smith, and A. Protat, 2018: A Prototype Method for Diagnosing High Ice Water Content Probability Using Satellite Imager Data. Submitted to *Atmos. Meas. Tech*, doi:10.5194/amt-11-1615-2018

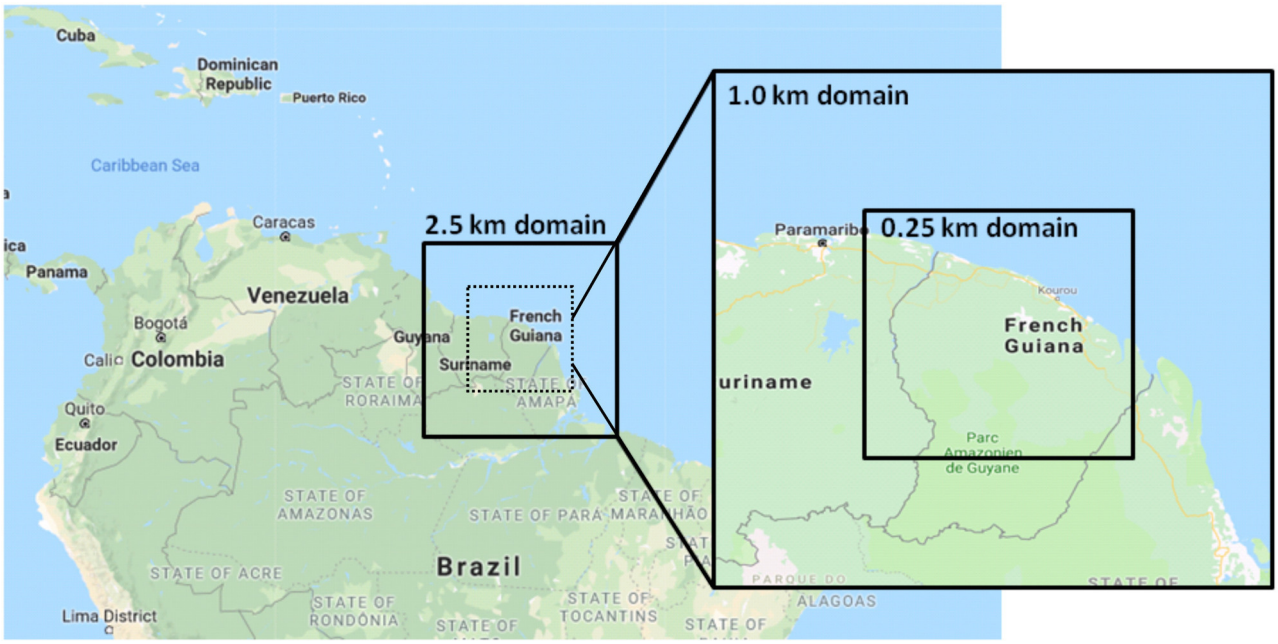

Fig.01.jpg

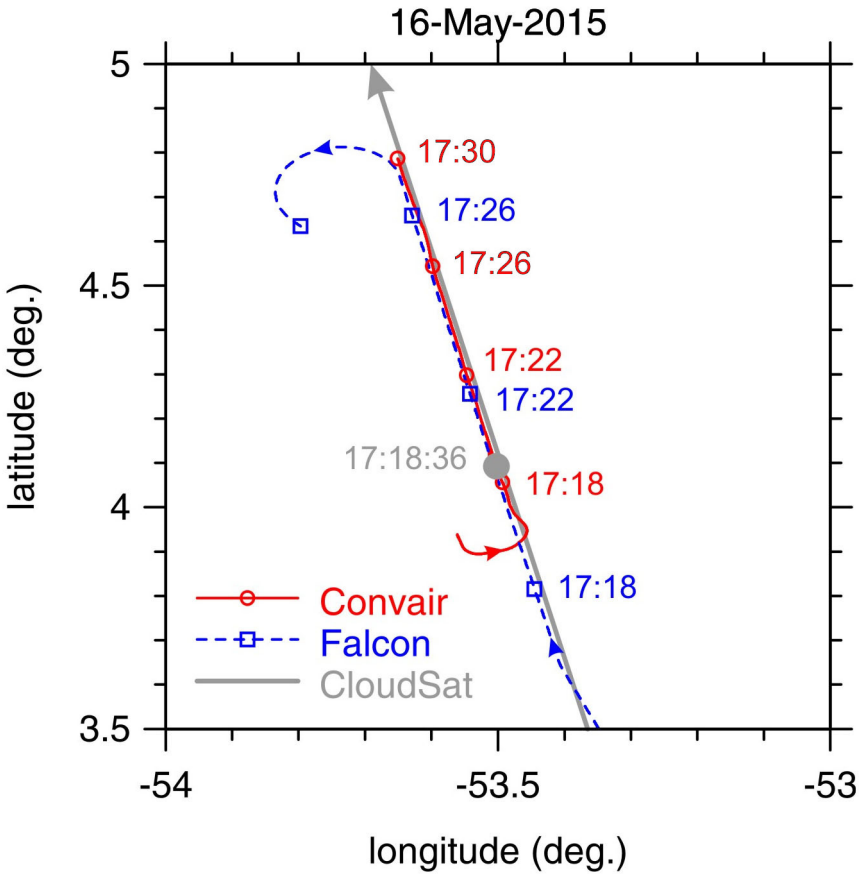

Fig.02.jpg

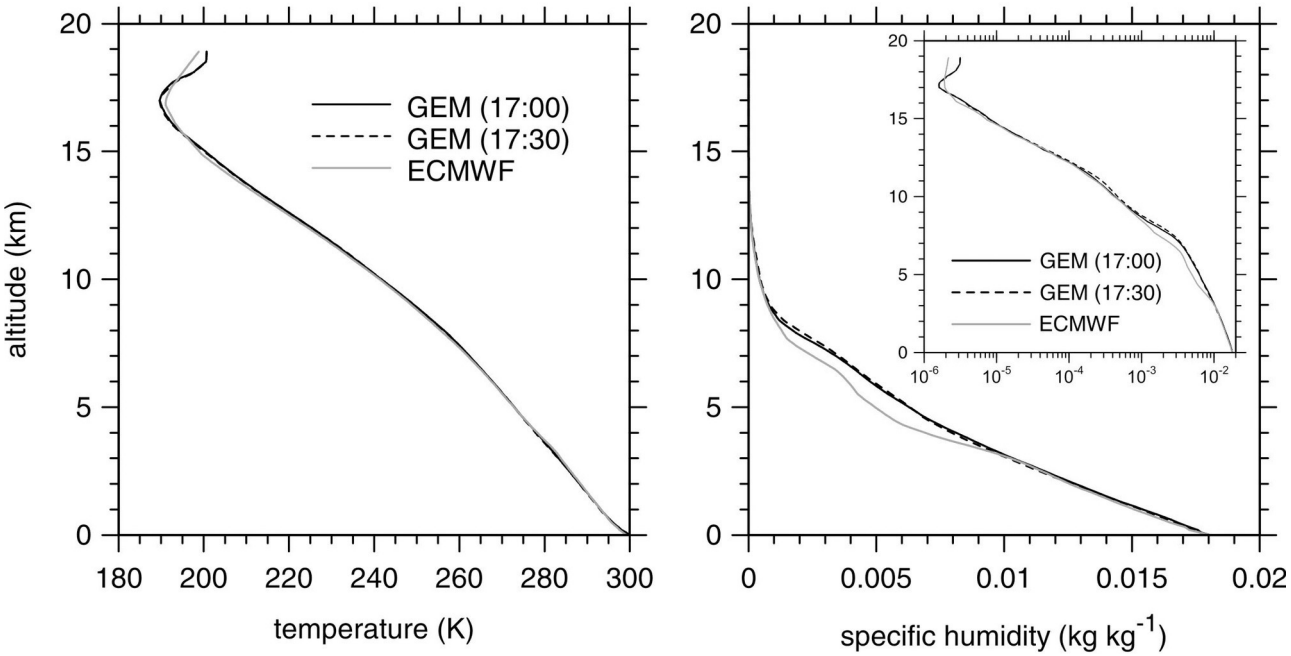

Fig.03.jpg

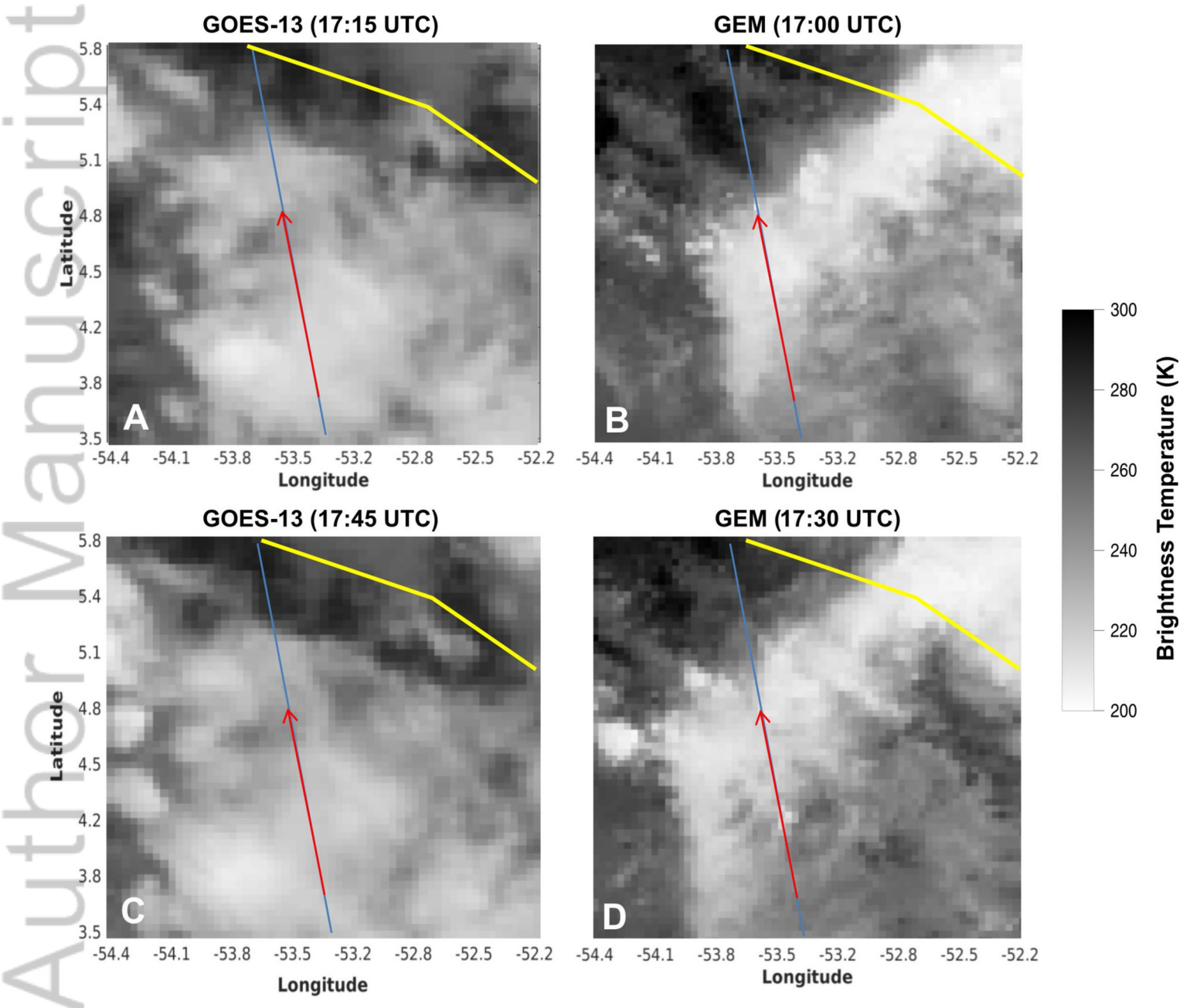

Fig.04.jpg

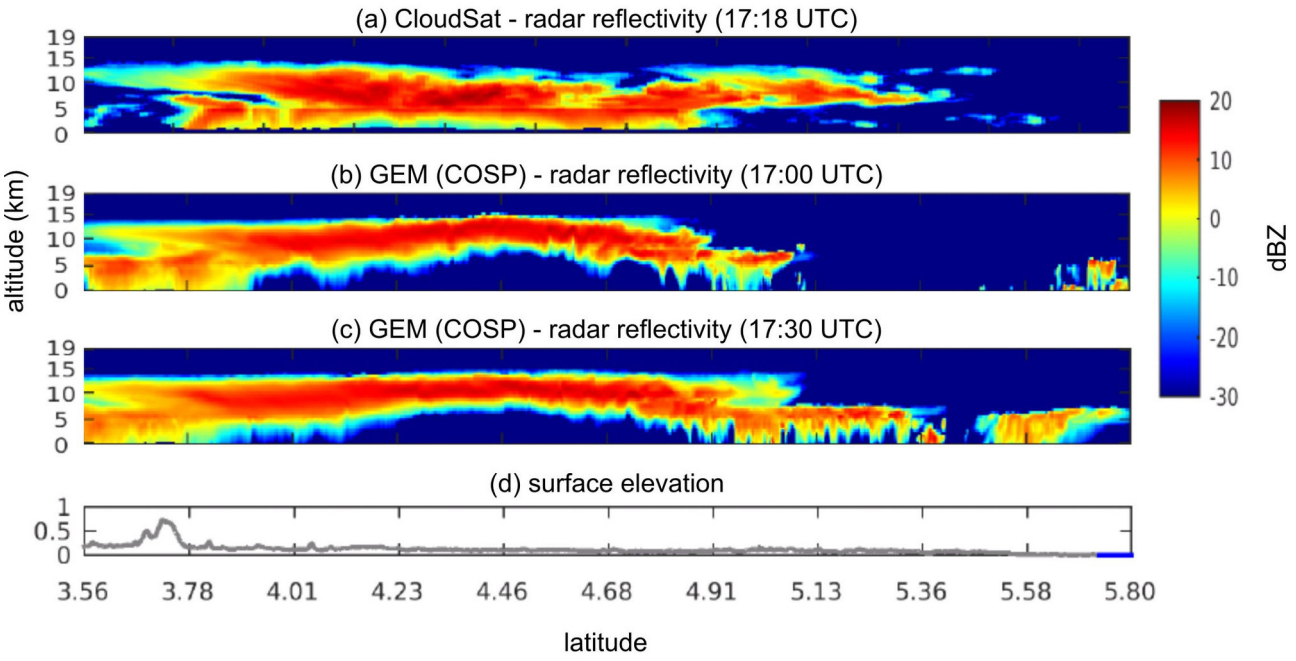

Fig.05.jpg

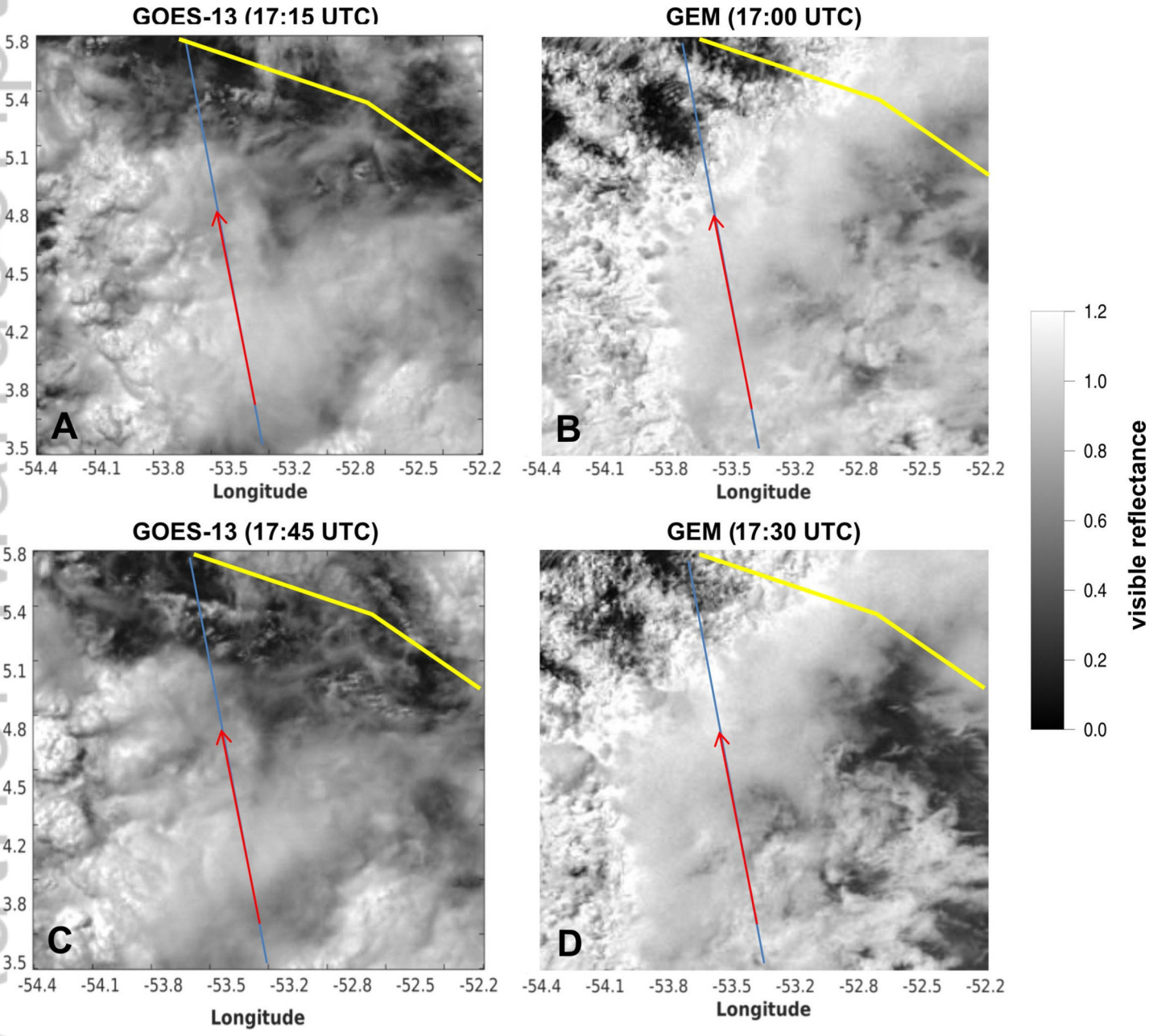

Fig.06.jpg

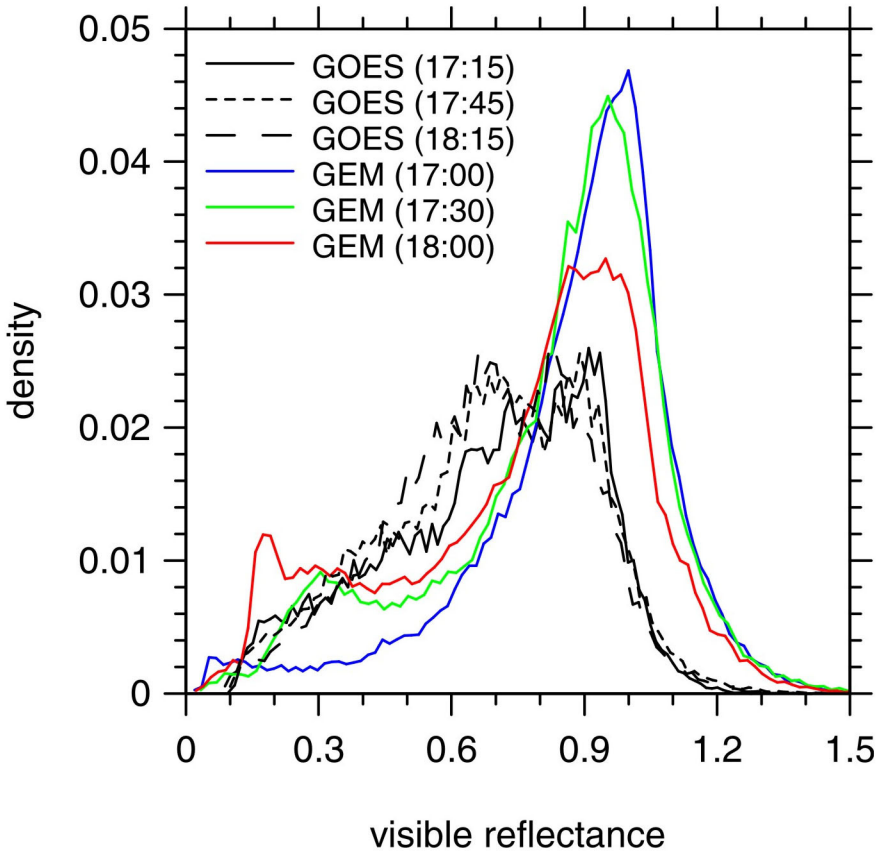

Fig.07.jpg

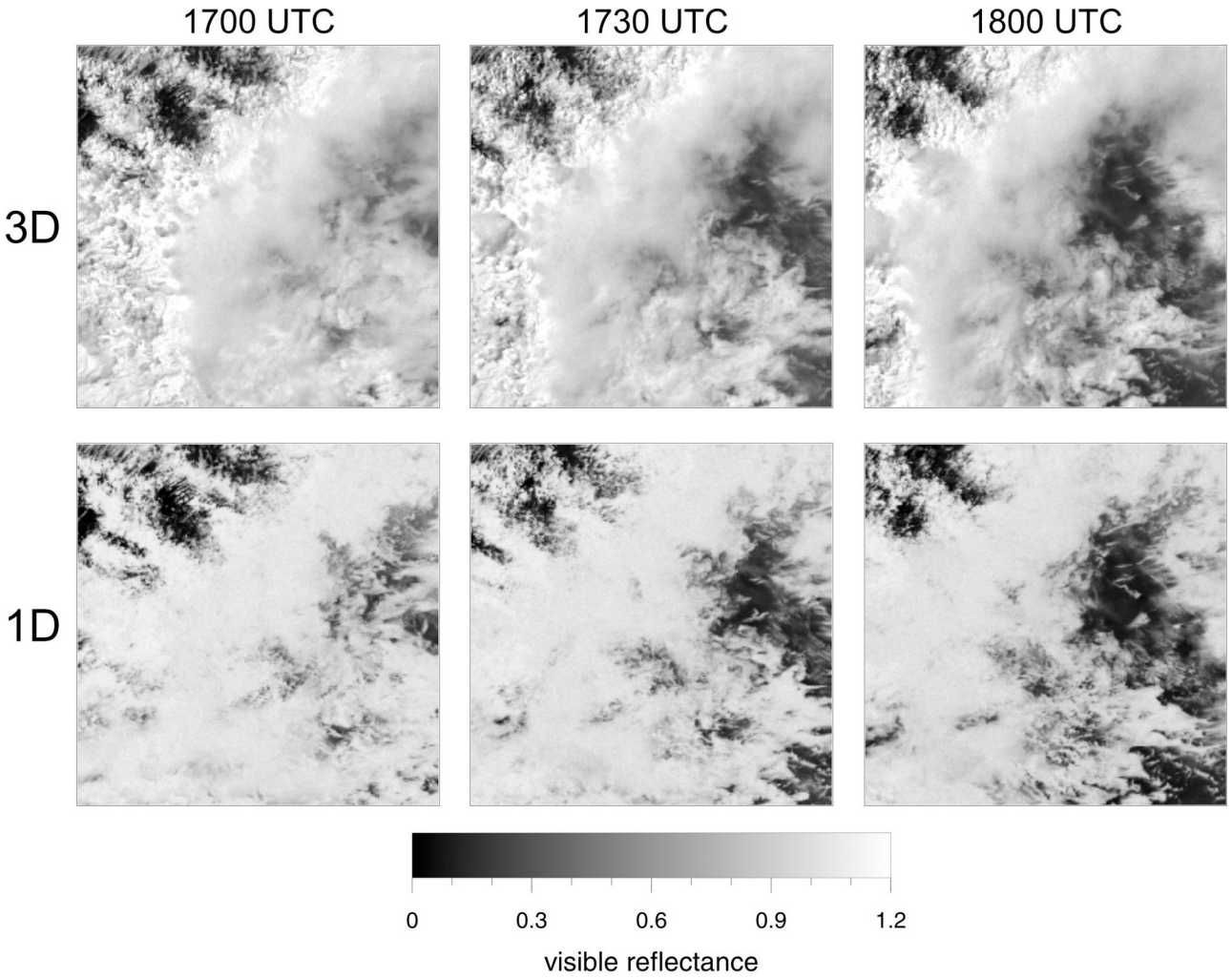

Fig.08.jpg

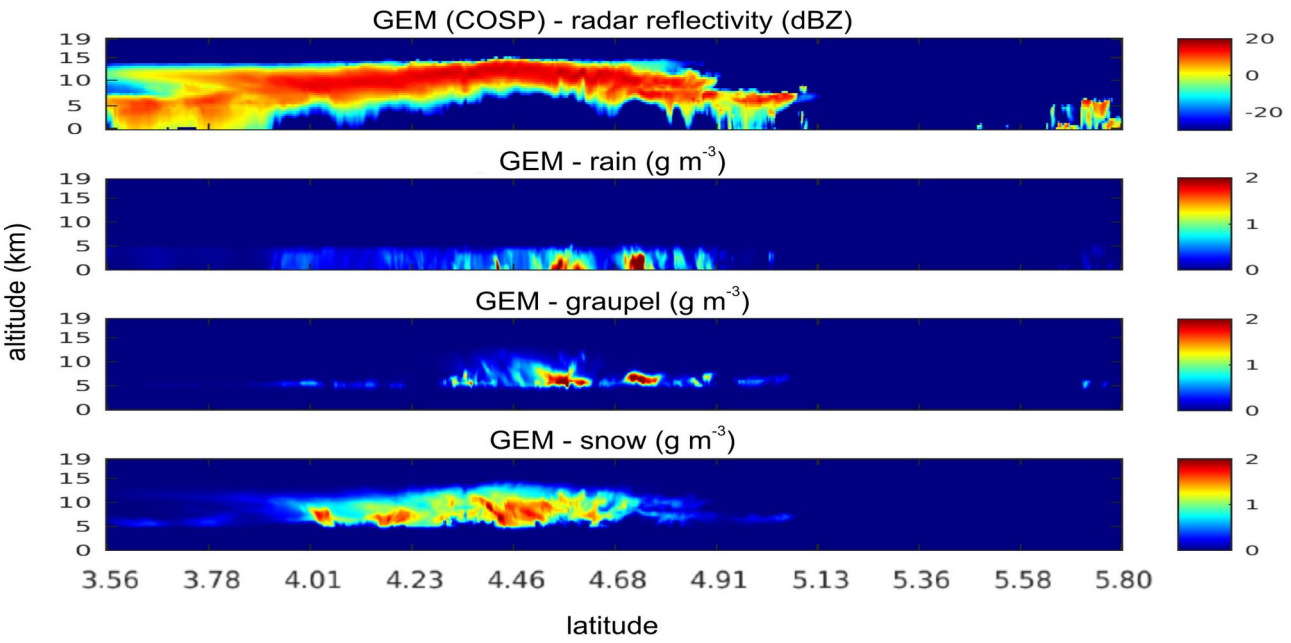

Fig.09.jpg

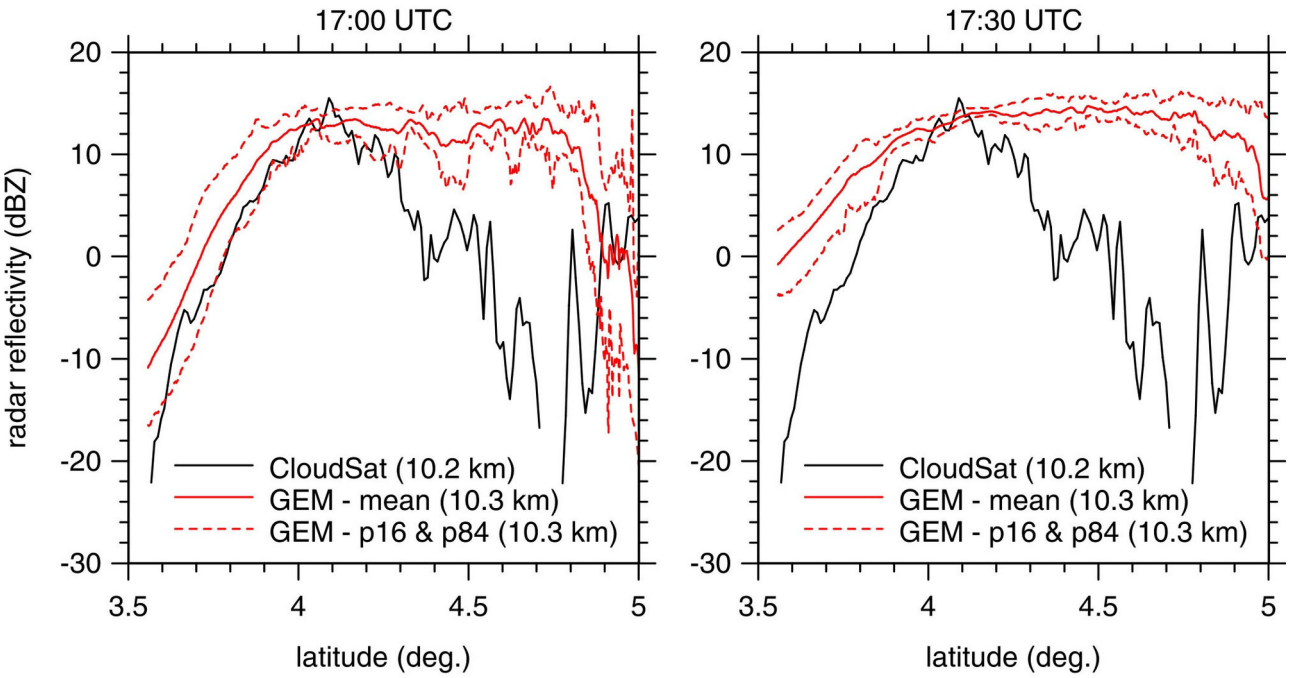

Fig.10.jpg

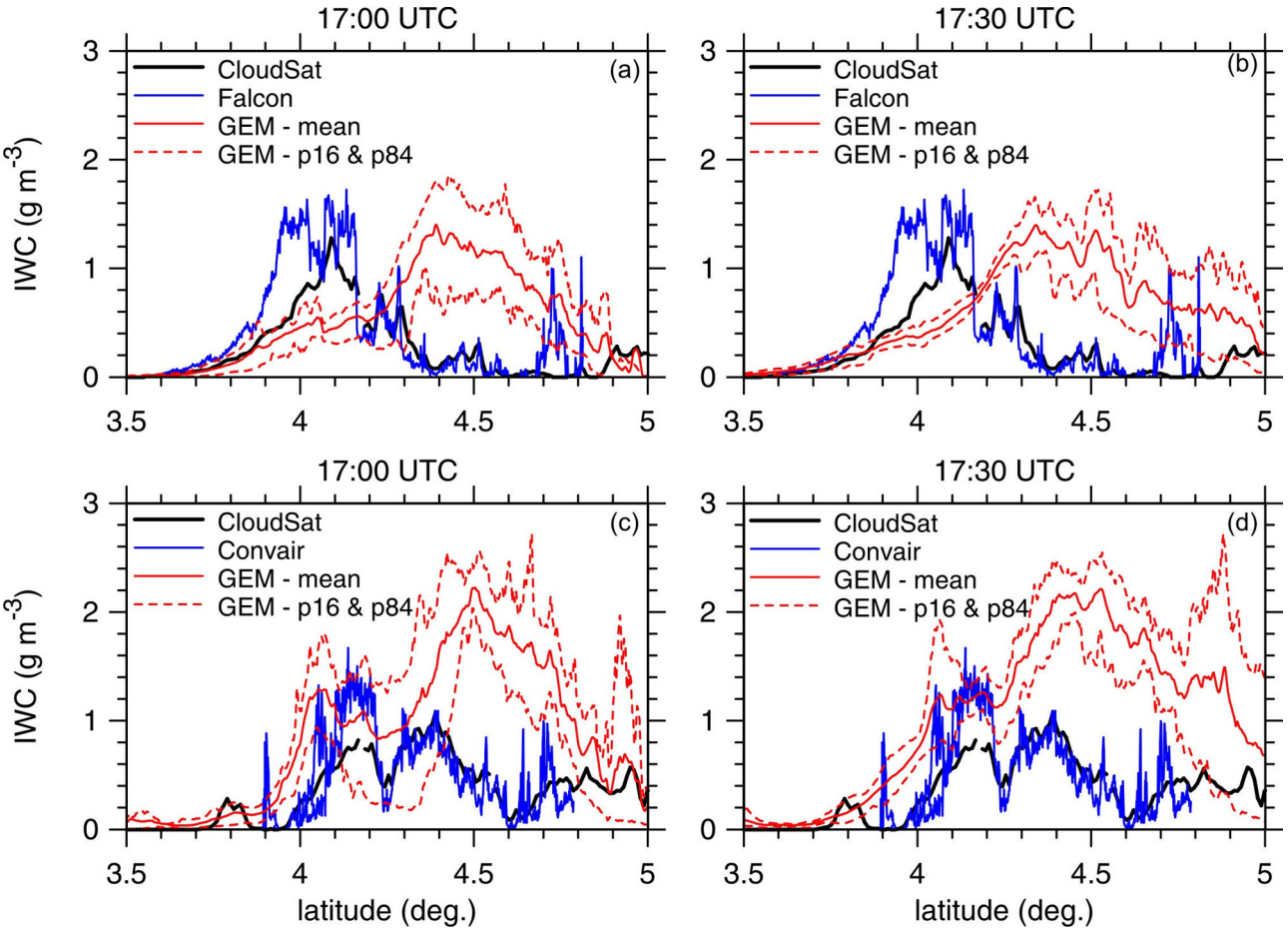

Fig.11.jpg

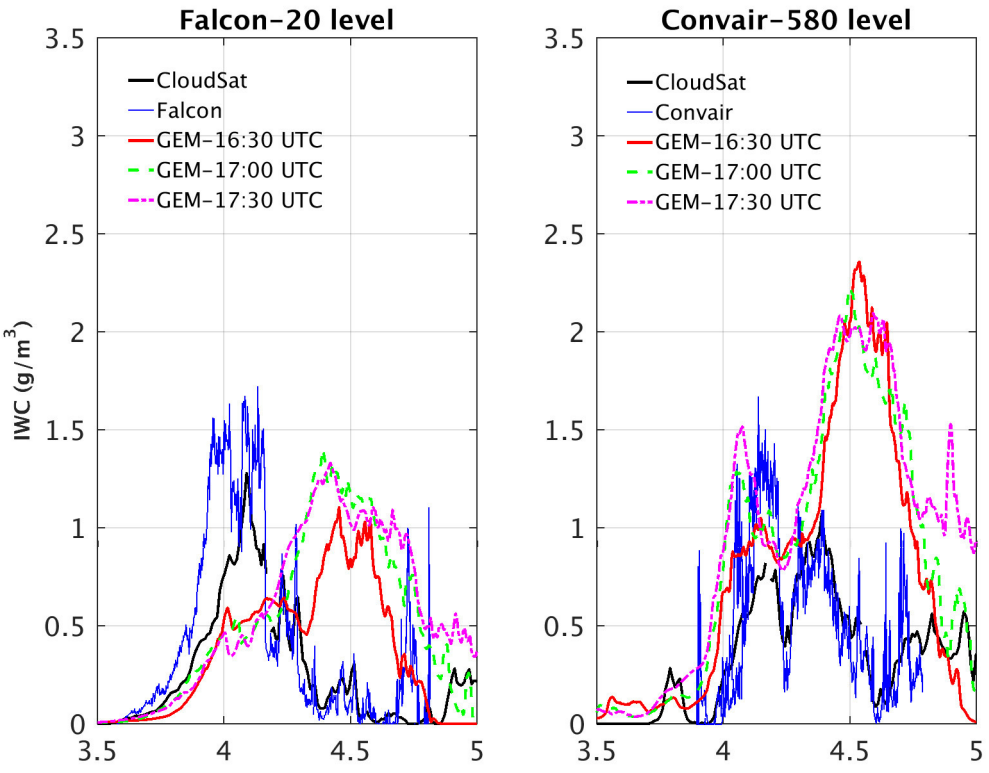

Fig.12.jpg

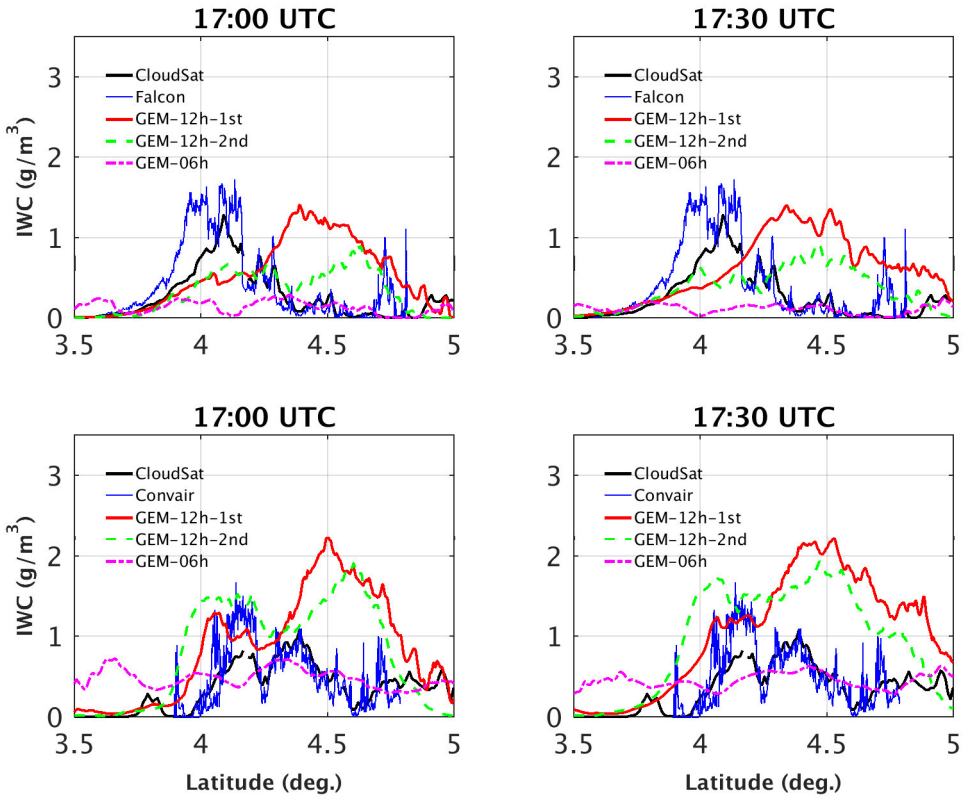

Fig.13.jpg

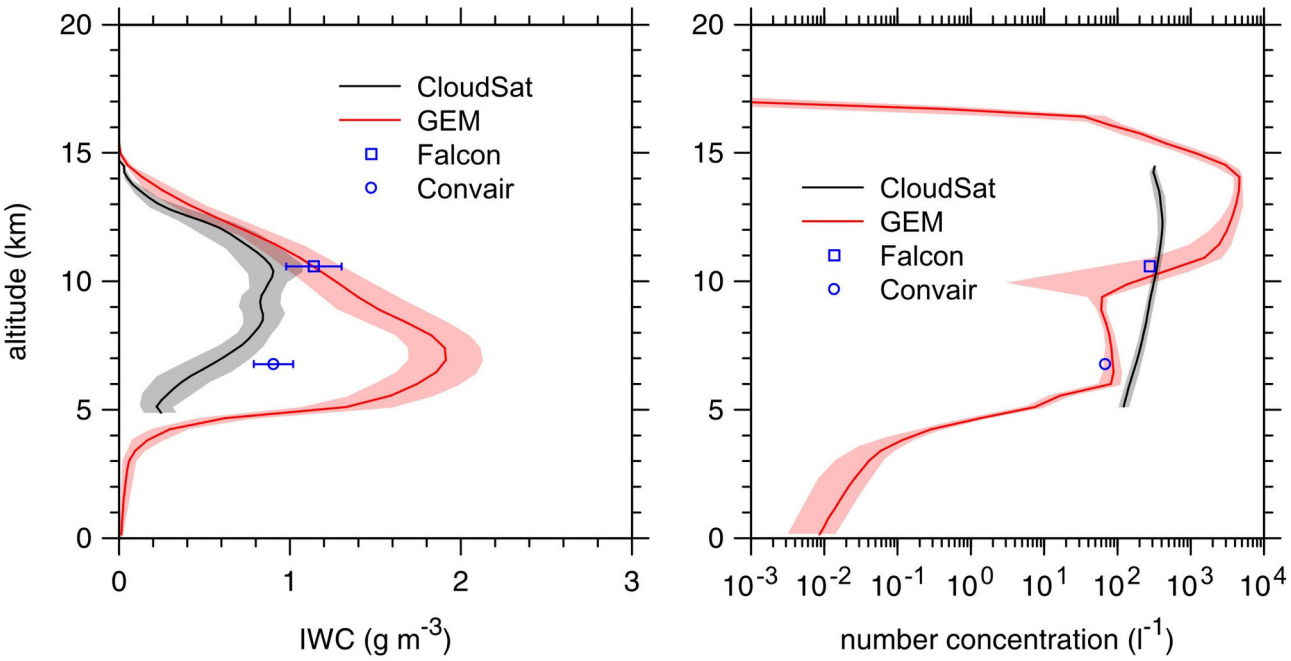

Fig.14.jpg

Evaluation of a high-resolution NWP model's simulated clouds using observations from CloudSat and *in situ* aircraft

ZHIPENG QU[1,8*], HOWARD W. BARKER[1], ALEXEI V. KOROLEV[1], JASON A. MILBRANDT[2], STEPHANE BELAIR[2], SYLVIE LEROYER[2],MENGISTU WOLDE[3], ALFONS SCHWARZENBÖCK[4], DELPHINE LEROY[4], J. WALTER STRAPP[5], JASON N. S. COLE[1], LOUIS NGUYEN[6], AND ANDREW HEIDINGER[7]

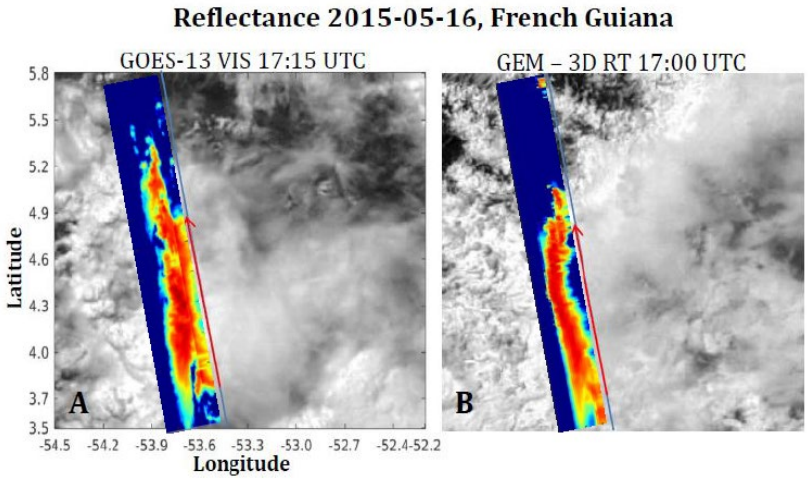

The tropical convective clouds generate high ice water content in high altitude which can compromise safe operation of commercial jet engines. This study evaluates the potentiality of high-resolution NWP model's capability of prediction the region with excessive ice water content. The results of this evaluation have also led to further considerations of the role of secondary ice processes in the modeling of cloud properties for tropical regions.